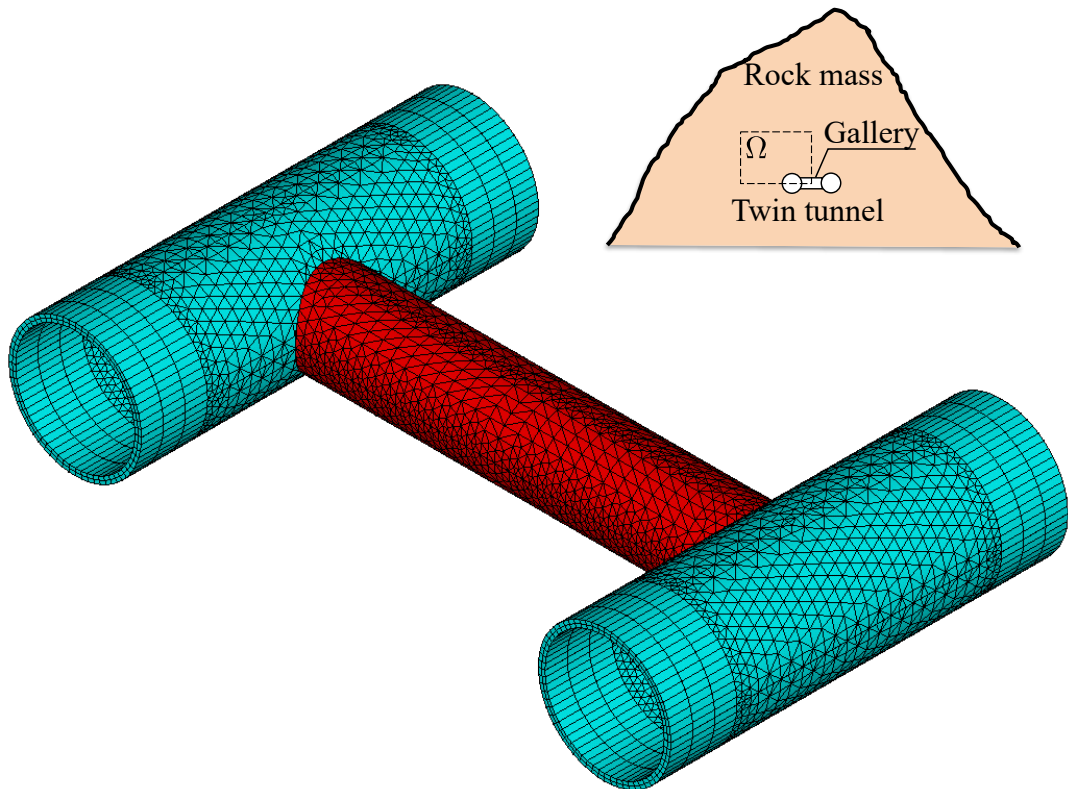


Graphical Abstract

Numerical analysis of the rock deformation in twin tunnels with transverse gallery considering plasticity and time-dependent constitutive models

Quevedo, F. P. M., Colombo, C. A. M. M., Bernaud, D., Maghous, S.



Highlights

Numerical analysis of the rock deformation in twin tunnels with transverse gallery considering plasticity and time-dependent constitutive models

Quevedo, F. P. M., Colombo, C. A. M. M., Bernaud, D., Maghous, S.

- Rock deformation in twin tunnels with transverse gallery is addressed by 3D computational.
- The irreversible behavior of the rock material is formulated in the context of coupled plasticity-viscoplasticity.
- Creep deformation of lining concrete is addressed by aging viscoelastic model.
- Numerical simulations emphasize the tunnel deformation anisotropy induced by twin tunnels proximity.
- High lining instantaneous stiffness can predominately control tunnel convergence and restrict interaction effects.

Numerical analysis of the rock deformation in twin tunnels with transverse gallery considering plasticity and time-dependent constitutive models

Quevedo, F. P. M.^{a,*}, Colombo, C. A. M. M.^a, Bernaud, D.^a and Maghous, S.^a

^aFederal University of Rio Grande do Sul, Av. Osvaldo Aranha, 99, Porto Alegre, 90.035-190, RS, Brazil

ARTICLE INFO

Keywords:

twin tunnels
transverse gallery
plasticity-viscoplasticity coupling
viscoelastic lining
finite element model

ABSTRACT

Resorting to a three-dimensional finite element framework, the paper investigates the instantaneous and long-term deformation in twin tunnels with connecting transverse gallery. Particular emphasis is dedicated to assessment of combined effects induced by time-dependent constitutive behavior of the material constituents and twin tunnels proximity, on the convergence profile. At the material level, the rock material mechanical behavior is formulated within the context of coupled plasticity–viscoplasticity, which proves relevant to the modeling and simulation of tunnel deformation in deep clayey rocks. A fundamental aspect of modeling the rock/support structure mechanical interaction is related to the proper consideration of time-dependent properties of the lining concrete material. In that respect, the concrete creep deformation is addressed by means of an aging viscoelastic model relying on the Bažant and Prasanna Solidification Theory, whereas shrinkage deformation component is accounted for by means of the formulation proposed in CEB-FIP MC90 standard. At the structure level, the deactivation-activation technique is employed in the three-dimensional computational model to simulate the excavation/advancing face and lining installation processes. The accuracy of the finite element predictions is assessed through comparisons with available analytical stress solutions formulated within a simplified setting for the twin tunnels configuration. The computational model is applied to analyze the short-term and long-term convergence profiles in a fully 3D twin tunnels configuration. A series of simulations varying some relevant parameters defining the structure geometry and constituents behavior are undertaken with the aim to give preliminary insight into the multiple interactions rising from twin tunnel proximity, intersecting transverse gallery and lining support. Numerical simulations have notably emphasized the deformation anisotropy induced by tunnels proximity as well as that peak convergence values are observed within a localized extension region close to tunnel-gallery intersection. Finally, the crucial role of time-dependent properties of concrete lining and related instantaneous stiffness in controlling the tunnel deformation is also studied.

1. Introduction

The increasing development of tunnel infrastructures for transportation systems and facilities networks in urban, hilly or underwater environments requires rational and efficient use of underground space, leading in many situations to tunneling nearby existing or new tunnels. The number of deep or shallow twin tunnels excavated in close proximity to each other has notably increased in the last years mainly due to prevailing underground and geotechnical conditions in congested urban areas. Resorting to the solution of twin tunnels, each branch being devised for a flow direction, also presents technical and safety advantages such as the reduction of tunnel diameter. Furthermore, in most cases of adjacent twin tunnels, the construction of connecting transverse galleries is a standard tunnel engineering practice either for safety (emergency exit/access) or functionality (maintenance, service cross-passage) purposes.

The sequence of construction phases of parallel twin tunnels running side-by-side as well as of the transverse gallery is generally dictated by the engineering practice and construction program. The tunnel junctions are usually

*Corresponding author.

✉ motta.quevedo@ufrgs.br (Q.F.P. M.); ca-colombo@hotmail.com (C.C.A.M. M.); denise.bernaud@ufrgs.br (B. D.); samir.maghous@ufrgs.br (M. S.)

✉ <https://www.researchgate.net/profile/Felipe-Pinto-Da-Motta-Quevedo> (Q.F.P. M.);
<http://lattes.cnpq.br/4919388217690564> (C.C.A.M. M.); <http://lattes.cnpq.br/2809615143819128> (B. D.);
<https://www.researchgate.net/profile/Samir-Maghous> (M. S.)

ORCID(s): 0000-0003-4171-1696 (Q.F.P. M.); 0000-0001-6365-3269 (B. D.); 0000-0002-1123-3411 (M. S.)

constructed far behind the advancing face of main tunnel to ensure the excavation of latter slightly affects that of the junction gallery [1,2]

In this context, understanding and assessing the multiple interactions between the components of such a tunnel material system, namely the closely-spaced twin tunnels, the intersecting transverse gallery, the support lining and the ground, is a fundamental and challenging engineering issue that should be handled during the planning stages for optimal design and safety of the whole tunneling operations. Evidence of interaction phenomena in twin tunnels and tunnel junctions have been reported by many case studies (e.g., 3, 3 4, 5, 6, 7, 8, 9,10, 11,12,13, 2]. From a structural design viewpoint, the analysis of the complex interaction in such a tunnel system is not an easy task since it inherently involves several factors related to geometry and constitutive characteristics as well as to the prevailing initial mechanical state and the sequence of tunneling. In particular, the computational evaluation of rock deformation and lining loading near the region of tunnel-gallery intersection requires a three-dimensional modeling (e.g., 14, Chortis and Kavvadas (2021)[12]). The construction process of the transverse gallery induces a stress redistribution within the surrounding rock mass, which in turn results in additional loading applied to the lining support of the main tunnel. Furthermore, a key aspect of the 3D modeling is the ability to capture the interaction effects on both short-term and long-term structural behavior, which are mainly controlled by the time-dependent rheological behavior of the rock and lining material constituents.

2. Fundamental assumptions

The basic assumptions of the constitutive and computational modeling, as well as related limitations, are summarized as follows:

- (a) Only the configuration of deep tunnels shall be considered in the subsequent analysis, thus neglecting deformations caused by surface loads and settlements arising from the excavation process.
- (b) Although material heterogeneity and behavior anisotropy are inherent features of soils and rocks, the rock mass is modeled throughout the paper as a homogeneous and isotropic continuous medium. At the scale adopted for tunnel modeling (macroscopic scale), this assumption means in particular that the possible micro-heterogeneities, such isotropic distributions of joints or cracks present at the finer scale, are accounted for in the homogenized behavior by means of a preliminary homogenization process (e.g., [15, 16, 17, 18, 19]). Clearly enough, the framework of continuum modeling adopted in the paper would reveal questionable when the rock mass is cut by a few macroscale fracture joints.
- (c) The rock mass is phenomenologically modeled using an elastoplastic-viscoplastic rheological law to capture instantaneous and long-term responses. This approach disregards the aspect connected temperature gradients, water flow, and poromechanics coupling.
- (d) Despite the complexity of the stress distribution prevailing in the rock mass before the process of tunnel excavation, which is mainly affected by the geological history, the present study assumes a geostatic initial stress reflected by vertical and horizontal stresses.
- (e) Twin tunnels are often designed considering a time gap between excavation fronts. However, the finite element simulations assume synchronous excavation steps to ensure symmetry conditions.
- (f) The simulation excavation processes are carried out assuming a constant tunnel advancement rate (i.e., constant excavation speed), together with a constant thickness of concrete lining.
- (g) Effects of temperature and humidity that may affect the viscoelastic behavior of lining concrete are disregarded.
- (h) Perfect bonding is assumed at the interface between concrete lining and the rock mass.
- (i) The framework of infinitesimal strain analysis, together with quasi-static evolutions, is adopted in the paper. In particular, dynamic excitations and related inertial forces, such as those induced, for instance, by earthquakes or explosions, shall not be considered in the numerical analysis.

3. Constitutive Model of the Rock Material

Time-dependent phenomena associated with the delayed behavior of the constitutive material are key aspects of deformation in tunnel structures excavated in deep clayey rocks (see for instance [20, 21] or [22], to cite a few). In most computational analyses developed for tunnel engineering design, this issue is generally addressed by means of viscoplastic constitutive behavior. While such constitutive models could relevantly model the transient and long-term

deformation, they seem however inadequate to capture the influence of short-term events (tunnelling and support placement phases) on the final stability of the structure. In particular, an analysis of tunnel deformation based on a viscoplastic model would suggest that the ultimate support pressure at tunnel structure equilibrium mainly depends on the closure rate at the moment when the contact between lining and rock mass is achieved (e.g., [21]), thus disregarding the irreversible effects rising in the initial construction phases. Indeed, during the primary stages of tunnel excavation, the surrounding rock mass is subjected to severe loading conditions and high strain rates, which may lead to yielding associated with high instantaneous irreversible strains near the tunnel wall, and can therefore affect the long-term equilibrium of the structure. It is thus of fundamental concern to formulate a constitutive model that incorporates both instantaneous and delayed irreversible components of the rock material. For this purpose, the present analysis considers a constitutive model that includes both instantaneous plasticity to describe shorth-term material yielding and viscoplasticity to represent delayed behavior. The formulation of the coupled plasticity-viscoplastic rheological model is based on that originally proposed in [21] and [20]. Previous studies have implemented this plastic-viscoplastic model for computational analysis of deformation in single tunnels (e.g., [23, 24, 22, 25]. For the sake of brevity, only the main features of this constitutive model shall be summarized below. Detailed description of the model, including application and validation in the context of single tunnel structures may be found in [26]. Finite element implementation of this model in the USERMAT procedure of ANSYS software is also described in [25].

The elastoplastic-viscoplastic model is formulated based on a serial association of the elastoplastic and viscoplastic constitutive models. The local strain rate $\dot{\epsilon}$ is split into three contributions $\dot{\epsilon} = \dot{\epsilon}^e + \dot{\epsilon}^p + \dot{\epsilon}^{vp}$, so that the constitutive relationships relating the Cauchy stress rate $\dot{\sigma}$ and strain rate components can be written as:

$$\dot{\sigma} = \mathbf{D} : \dot{\epsilon}^e = \mathbf{D} : (\dot{\epsilon} - \dot{\epsilon}^p - \dot{\epsilon}^{vp}). \quad (1)$$

In the above relationship, $\dot{\epsilon}^e$, $\dot{\epsilon}^p$ and $\dot{\epsilon}^{vp}$, represent respectively the elastic, plastic and viscoplastic strain rate, and \mathbf{D} denote the fourth-order isotropic elastic linear constitutive tensor. Tensor \mathbf{D} is defined by the rock mass elastic Young modulus E and Poisson ratio ν . The one-dimensional representation of the constitutive behavior is shown in Fig. 1.

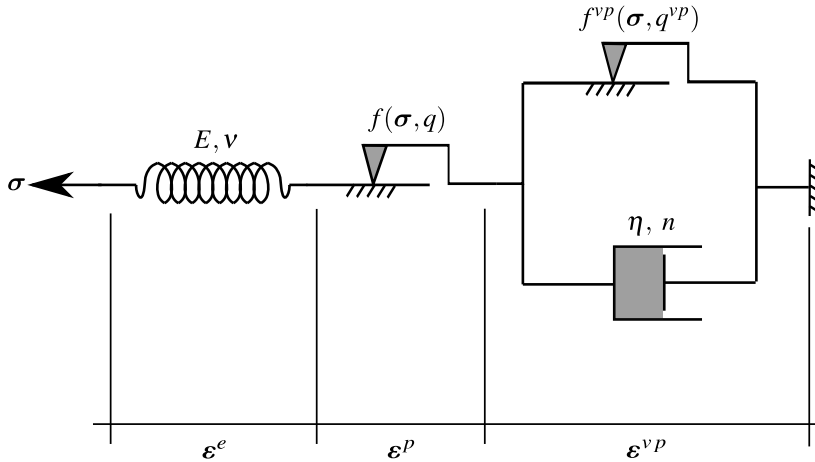


Figure 1: Rheological representation of the elastoplastic-viscoplastic model.

In the three-dimensional context, the plasticity component of constitutive behavior is described by a Drucker-Prager plastic flow surface given by:

$$f(\sigma, q) = f(I_1, J_2, q) = \beta_1 I_1 + \beta_2 \sqrt{J_2} - q(\alpha), \quad (2)$$

which I_1 is the first invariant of the stress tensor, J_2 the second invariant of the deviator tensor and β_1, β_2 and $q(\alpha)$ are strength parameters related to the friction angle ϕ and cohesion $c(\alpha)$, respectively. Drucker-Prager plasticity surface inscribed to the Mohr-Coulomb surface shall be considered throughout the subsequent analysis [27]:

$$\beta_1 = \frac{(k-1)}{3}, \quad \beta_2 = \frac{(2k+1)}{\sqrt{3}}, \quad q(\alpha) = 2\sqrt{k} c(\alpha), \quad (3)$$

where $k = (1 + \sin \phi)/(1 - \sin \phi)$. The internal variable α is the equivalent plastic strain $\bar{\varepsilon}^p$ used to simulate strain hardening/softening phenomena. However, for this study, we adopt perfect plasticity, meaning that c is a constant. For the viscoplasticity surface f^{vp} the same surface is employed, but with ϕ^{vp} in β_1 and β_2 , and $q^{vp} = 2\sqrt{k^{vp}} - c^{vp}$ where $k^{vp} = (1 + \sin \phi^{vp})/(1 - \sin \phi^{vp})$ and c^{vp} is a constant, i.e., perfect viscoplasticity. The plastic flow rule is given by:

$$\dot{\varepsilon}^p = \begin{cases} \lambda \frac{\partial g}{\partial \sigma} & \text{for } f > 0 \\ 0, & \text{for } f \leq 0 \end{cases}, \quad (4)$$

where λ is the plasticity multiplier and g is a potential flow function analogous to f used to simulate the volume dilatation during the evolution of plastic deformations. However, for this analysis, was used associated plasticity, i.e., $g = f$. The plastic multiplier is obtained through the consistency condition $\dot{f} = 0$. Numerical details of this implementation can be found in [26]. For viscoplastic flow rule we have,

$$\dot{\varepsilon}^{vp} = \lambda^{vp} \frac{\partial f^{vp}}{\partial \sigma} \quad (5)$$

In contrast to the plastic multiplier, the viscoplastic multiplier λ^{vp} is independent of a consistency like condition. As a result, its expression is explicit. Based on the framework of generalized Perzyna's overstress theory [28], its expression may be derived as follows:

$$\lambda^{vp} = \frac{\Phi(\sigma, q^{vp})}{\eta} \quad \text{and} \quad \Phi = \left\langle \frac{f^{vp}(\sigma, q^{vp})}{f_0} \right\rangle^n, \quad (6)$$

where Φ is the overstress function, η is the dynamic viscosity constant, n is the dimensionless parameter that gives the form of the power law, f_0 a parameter conveniently adopted and $\langle * \rangle$ is the McCauley function which is 0 when $* < 0$, i.e. viscoplastic flow will only occur when the overstress function is positive.

In this coupled model, when $\phi = \phi^{vp}$, cohesion entirely controls the evolution of local mechanical fields. Specifically, when $c \rightarrow \infty$ and $c^{vp} \rightarrow \infty$, the system achieves a purely elastic solution. The solution becomes purely elastoviscoplastic with $c \rightarrow \infty$, while a pure elastoplastic solution emerges with $c^{vp} \rightarrow \infty$. In the coupled analysis, condition $c^{vp} < c$ is adopted, allowing the viscoplastic domain to occur without plasticity. However, in the presence of plasticity, viscous effects become inevitable. Fig. 2 illustrates these domains in principal stress space.

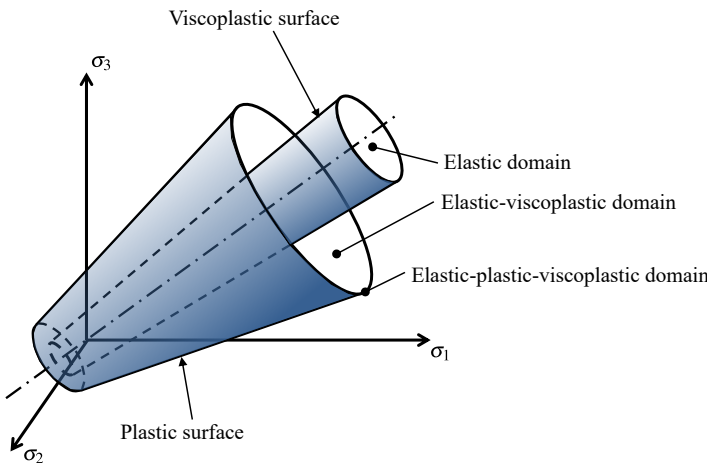


Figure 2: Elastoplastic-viscoplastic domains.

4. Constitutive Model of the Lining

Shrinkage and creep phenomena represent fundamental components of concrete deformation processes that are expected to naturally affect the instantaneous as well as the transient and long-term behavior of structures involving

such material. However, most of the tunnel design analyses consider the concrete involved in lining systems as a linear elastic material. From a phenomenological point of view, creep of concrete refers to the time-dependent deformation induced by sustained loading, whereas shrinkage deformation refers to the volume decrease caused by drying. As far as deformation in tunnel structures is concerned, creep and shrinkage have an important effect on the performance of the concrete lining and consequently on its contribution to controlling the long-term convergence of the tunnel. To account for such constitutive features, the concrete creep deformation is addressed by means of an aging viscoelastic rheological model relying on Bažant and Prasannan Solidification Theory [29, 30]. The viscoelastic model is described by a Generalized Kelvin-chain as depicted in Fig. 3. The mechanical parameters that define such a rheological model are the springs stiffness and dash-pots viscosity. The model parameters are calibrated based on the CEB-FIP MC90 standard specifications formulation reported in [31]. One may refer to [32, 33] for detailed description of the calibration procedure. As regards the concrete deformation associated with shrinkage, the isotropic formulation proposed in CEB-FIP MC90 standard [31] is adopted in the present modeling and subsequent computational analyses. Full details regarding model definition and related finite element implementation may be found in [34] and [33].

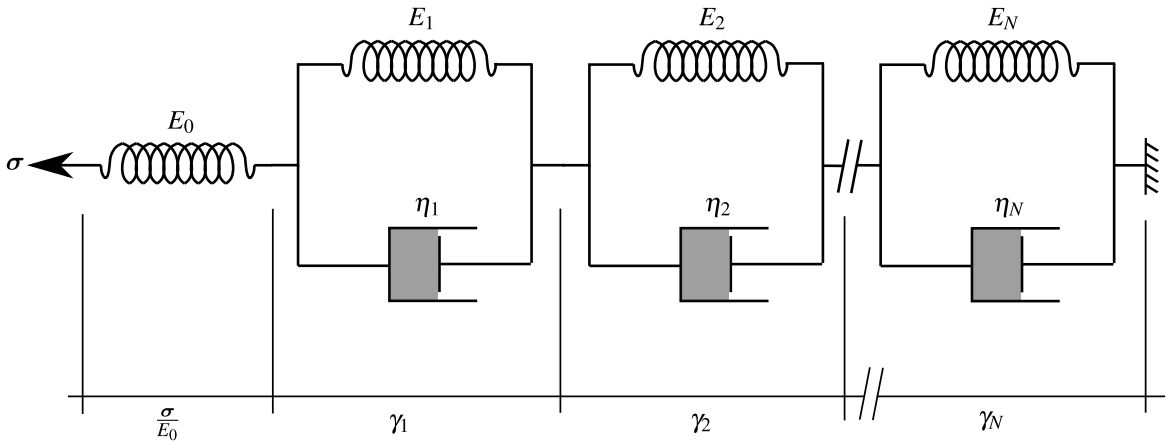


Figure 3: Generalized Kelvin model for uniaxial concrete viscoelasticity.

Accordingly, the constitutive equations for concrete lining relating the stress and strain rate can be expressed in the framework of infinitesimal strain analysis as:

$$\dot{\sigma} = \mathbf{D} : \dot{\epsilon}^e = \mathbf{D} : \dot{\epsilon} - \mathbf{D} : \dot{\epsilon}^{sh} - \mathbf{D}^* : \dot{\epsilon}^{cr} \quad (7)$$

In the above relationship, $\dot{\epsilon}^{sh}$ and $\dot{\epsilon}^{cr}$ are respectively the shrinkage and creep strain rates. The fourth-order tensors \mathbf{D} and \mathbf{D}^* refer to the isotropic elastic linear constitutive tensor and modified constitutive tensor that incorporate the aging viscoelastic properties of the concrete, respectively.

For the numerical implementation purposes, relationship (12) may conveniently be written in incremental form:

$$\Delta\sigma = \mathbf{D} : \Delta\epsilon - \mathbf{D} : \Delta\epsilon^{sh} - \mathbf{D}^* : \Delta\epsilon^{cr} \quad (8)$$

As mentioned above, isotropic formulation is considered for shrinkage, so that increment of shrinkage strain reads:

$$\Delta\epsilon^{sh} = \Delta\epsilon_{sh}(t_s)\mathbf{1} \quad (9)$$

where t_s represents the concrete curing time, and $\Delta\epsilon_{sh}$ is the variation in magnitude of the concrete deformation associated with shrinkage (the dependency $\Delta\epsilon_{sh}$ of on current time is omitted). The latter expression is determined based on CEB-FIP MC90 standard specifications [31].

Regarding the increment of creep strain $\Delta\epsilon^{cr}$, its value is computed making use of the incremental algorithm developed by Bažant and Prasannan [29, 30], together with a model calibration that incorporates CEB-FIP MC90 standard formulation [31]. More precisely, the three-dimensional ageing viscoelastic behavior of isotropic concrete is defined by the Generalized Kelvin model for the relaxation modulus under uniaxial stress, whereas the Poisson

ratio is assumed to be time independent within the time interval of analysis. The procedure for the identification of model parameters is achieved by comparing the creep functions provided in references [29, 30] and [31], leading to the following equivalence:

$$E_0 = E_c(t_0), \gamma(t - t_0) = \beta_c(t - t_0), \frac{1}{v(t)} = \frac{\phi_0(t_0)}{E_{ci}} \text{ and } \frac{1}{\eta(t)} \rightarrow 0 \quad (10)$$

in which t refers to the current time value and t_0 to the concrete age at the instant of load application (time interval $t - t_0$ is generally referred to as loading time or loading age). In the Generalized Kelvin model introduced by Bažant and Prasannan [29, 30], E_0 is the instantaneous elasticity modulus of the concrete formed aggregates and cement paste particles, $\gamma(t - t_0) = \sum_{i=1}^N \gamma_i$ is the microviscoelastic deformation of the volume fraction $v(t)$ of solidified concrete and $\eta(t)$ is the apparent macroscopic viscosity. In the CEB-FIP MC90 formulation [31], $E_c(t_0)$ stands for the tangent elastic modulus of concrete at the instant of the loading application t_0 , $\beta_c(t - t_0)$ is a coefficient that depends on the loading age $t - t_0$, $\phi_0(t_0)$ is a coefficient defining the delayed strain when loaded at age t_0 of the concrete, and E_{ci} represents the tangent elasticity modulus of the concrete at the age of 28 day.

5. Spatial and time discretization of the domain

The geometry model of analyzed domain Ω is schematically displayed in Fig. 4. It consists of a system of deep twin tunnels connected with a transverse gallery. The radius of the circular longitudinal tunnels is denoted by R_t , whereas that of the circular connecting gallery is denoted by $R_g \leq R_t$. The underground structure is excavated in a homogeneous rock mass at great depth $H \gg R_t$.

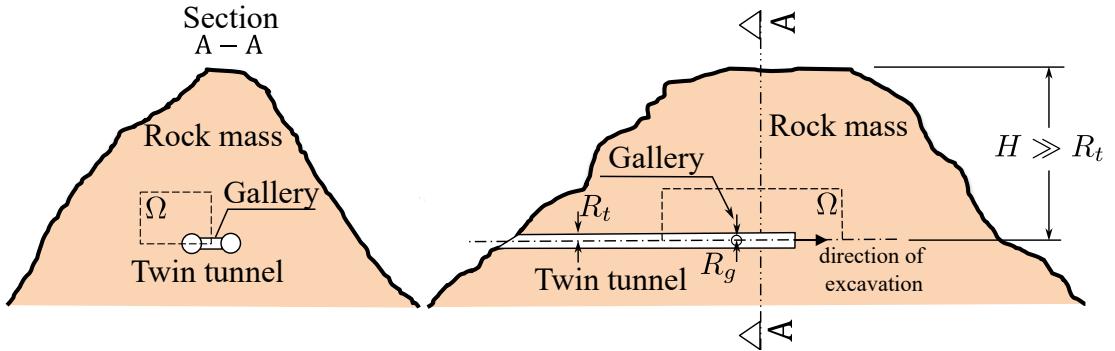


Figure 4: Schematic representation of the twin tunnels geometry problem.

Within the analyzed material domain, the initial stress state prevailing in the rock mass prior to the tunnel excavation process is defined by constant vertical and horizontal geostatic stress σ_v and σ_h , taking the following form:

$$\sigma_0 = -\sigma_v e_y \otimes e_y - \sigma_h (1 - e_y \otimes e_y) \quad (11)$$

where e_y is the upward unit vector parallel to vertical direction. The initial horizontal stress is generally related to the vertical stress by means of the horizontal thrust coefficient $\sigma_h = k_0 \sigma_v$. Starting from the initial configuration of the material system Ω , the processes of excavation (advancing face) and lining placement are simulated by means of the “activation/deactivation” technique [35, 36, 37, 33].

The geometry material domain Ω considered for the finite element simulations, including tunnelling and deformation analysis, is defined by a parallelepiped volume of dimensions $(L_1 + L_2) \times L_3 \times d_3$ (Fig. 5). Owing to the symmetry of the problem, only the material domain $\{x \leq 0, y \geq 0\}$ is considered for F.E discretization and analysis. Referring to the notations of Fig. 5, d_1 is the distance between the axes of longitudinal tunnels, L_2 represents the total length along longitudinal direction e_z of the cylindrical volume to be excavated that is considered in the numerical simulation, d_3 is the thickness along vertical direction e_y of material domain Ω , L_1 stands for the length of unexcavated region after total excavation process, L_3 is the total length along transversal direction e_x of discretized material domain, d_2 characterizes

the location of the circular transverse axis gallery that intersects the longitudinal tunnel at $z = L_1 + d_2$. The length of the excavation step adopted will be denoted by L_{pt} . The finite element model including geometrical discretization and boundary conditions is illustrated in Fig. 5. The mesh used in the simulations consists of 119740, 182470 or 221104 total elements (hexahedra and tetrahedra), depending on the value of spacing between longitudinal tunnels. To increase the accuracy of the model predictions in the intersection zone, the region surrounding the transverse gallery (including part of the longitudinal tunnel) is discretized by means 10-node quadratic tetrahedral elements, whereas 8-node trilinear hexahedral elements are used for the remaining part of the structure. Furthermore, a refined meshing is used for discretizing the zones surrounding the longitudinal and transverse gallery. These zones whose mechanical state is significantly affected by the tunnelling process are indicated by light gray color in Fig. 5.

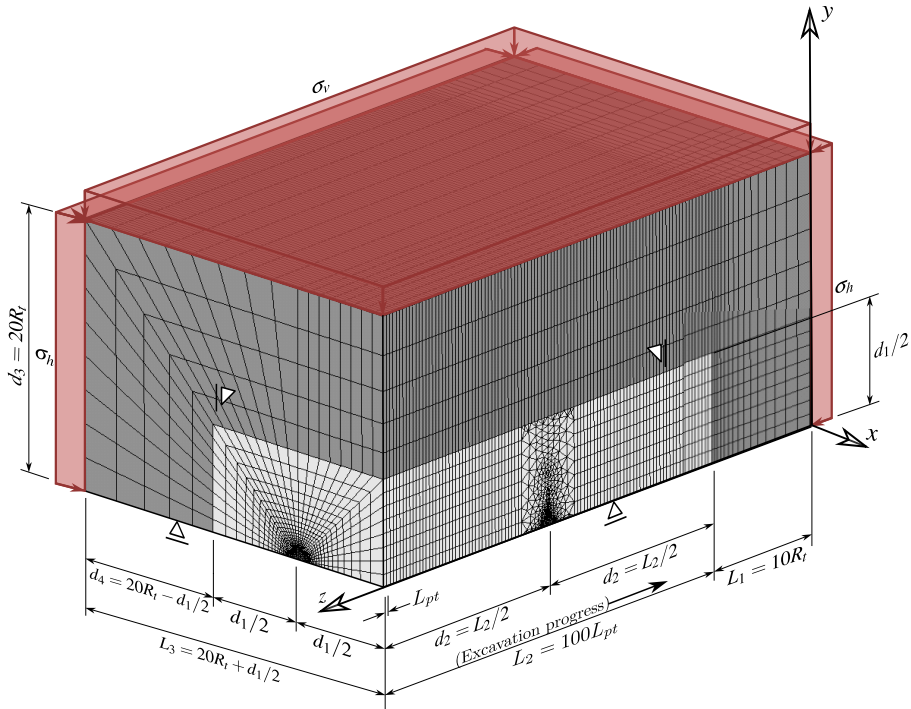


Figure 5: Mesh, dimensions and boundary conditions of the 3D twin tunnel domain.

Figures 6 to 10 display some details regarding the geometry and F.E discretization of the structure. Fig. 6 presents some details of the longitudinal tunnel cross-section in a xy plane, together with the layer of concrete lining (in sky blue color), parameter e_t being the thickness of the lining. Installation of the lining (shotcrete or precast concrete) is simulated in the F.E modeling by progressive activation of the corresponding elements, which consists in assigning to these elements the concrete mechanical properties.

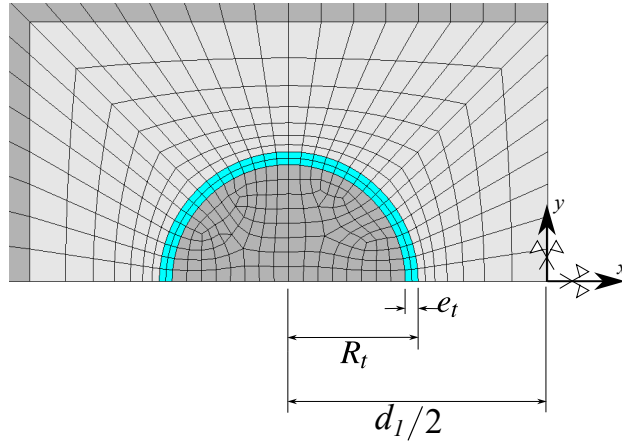


Figure 6: Detail 1 - Mesh in longitudinal tunnel cross-section with spacing $d_1 = 4R_t$.

An important issue investigated in this work is the influence of the spacing d_1 between twin tunnels on their convergence. Fig. 7 and Fig. 8 illustrate the spatial discretization of the gallery region as well as of the connection with the longitudinal tunnel. Three values shall be considered for the spacing d_1 in the numerical simulations, namely $d_1 = 16R_t$, $8R_t$ and $4R_t$. The layer of concrete lining of thickness e_g installed along the gallery wall is indicated by red color in the figures. Without introducing additional modeling restriction and for the sake of simplicity, the value of the gallery radius is fixed to $R_g = 2/3R_t$. The same lining system (same concrete material and layer thickness) is considered for both longitudinal tunnels and gallery. As regards the discretization of the region surrounding the gallery, parameters d_5 and d_1 define the size in a yz plane of the transition region involving the tetrahedral finite elements. Fig. 9 provides a view of the transition region and tunnel/gallery intersection zone.

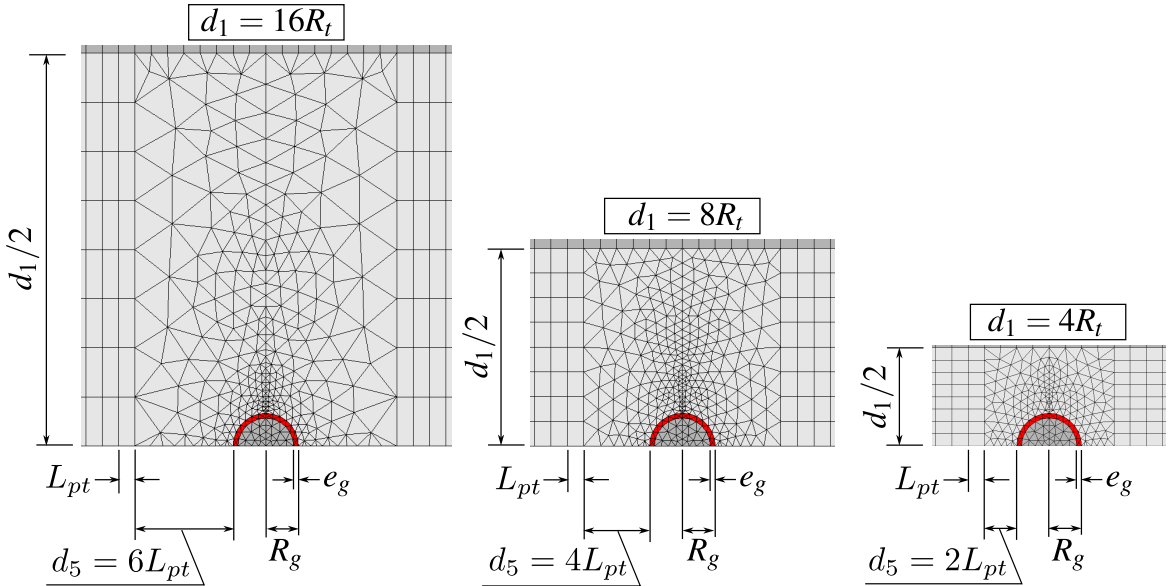


Figure 7: Geometry and F.E. mesh of gallery cross-section for configurations $d_1 = 16R_t$, $d_1 = 8R_t$ and $d_1 = 4R_t$.

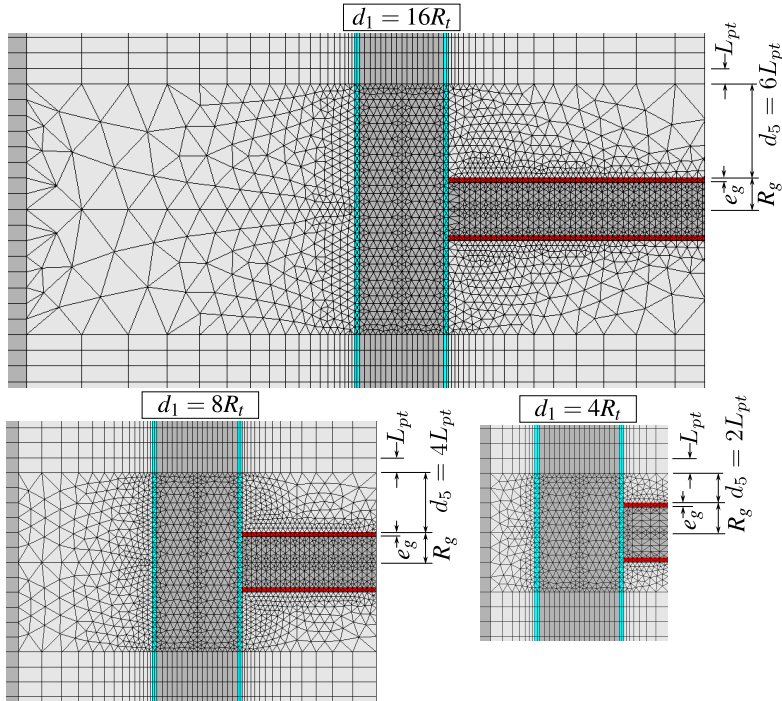


Figure 8: Views of longitudinal tunnel and gallery in the symmetry plane $y = 0$ for configurations $d_1 = 16R_t$, $d_1 = 8R_t$ and $d_1 = 4R_t$.

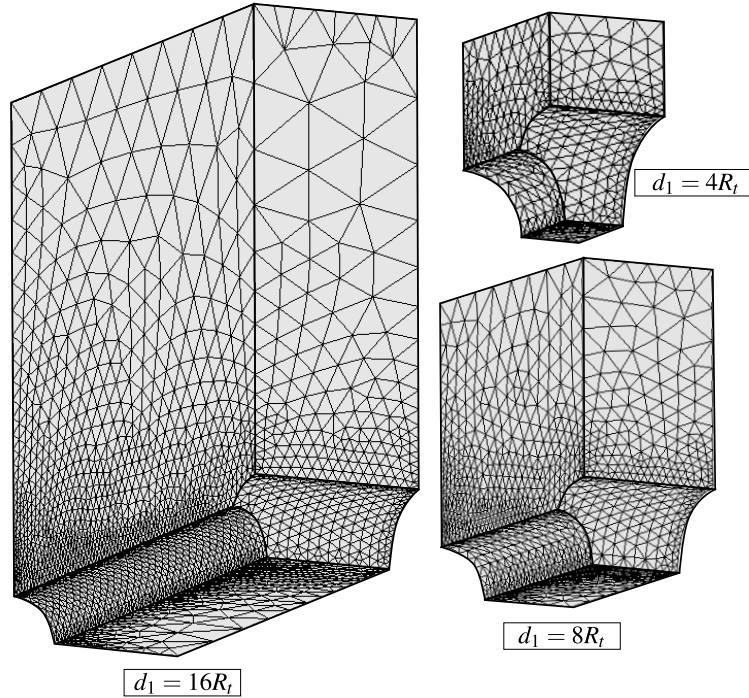


Figure 9: View of the transition and tunnel/gallery intersection zones for configurations $d_1 = 16R_t$, $d_1 = 8R_t$ and $d_1 = 4R_t$.

Finally, Fig. 10 presents the F.E mesh used for the layer of concrete lining in both the longitudinal layer (in sky blue color) and the gallery (in red color) for the three configurations $d_1 = 16R_t$, $d_1 = 8R_t$ and $d_1 = 4R_t$, with specific

details on the junction region of the gallery and the longitudinal tunnel. For the illustration purposes, symmetry with respect to plane $y = 0$ has been used to complete the geometry representation of each configuration. It is emphasized that the tetrahedral elements used for the discretization of the region surrounding the transverse gallery exactly fits excavation steps (elements removal or deactivation).

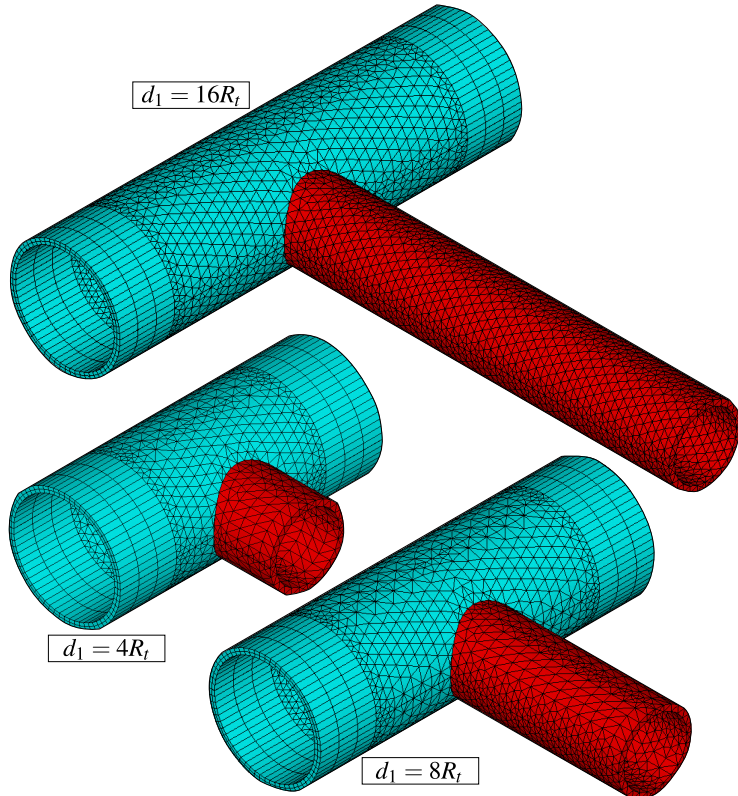


Figure 10: Isometric view of the lining at the intersection for $d_1 = 16R_t$, $d_1 = 8R_t$ and $d_1 = 4R_t$ - expansion of symmetry in the xz plane.

As mentioned previously, the tunnelling process, including the excavation steps and lining installation, is simulated resorting to the activation-deactivation method. Each excavation step is modeled by deactivation of the corresponding elements (the elements stiffness is reduced by a factor $1E8$), whereas installation of elements of lining at a distance d_{0t} from the excavation face (unlined length) is achieved through activation of the corresponding elements by assigning them concrete properties. The F.E solution of the time-dependent problem is performed for each excavation step associated with time interval $t_p = L_p/V_p$, where L_{pt} represents the length of the excavation step and V_{pt} is the speed of the excavation face. Fig. 11 schematically displays the consecutive phases of excavation process. In this Figure, n_p is the total number of excavation steps and n_{pig} represents the number of longitudinal tunnel excavation steps prior to gallery excavation. After achievement of the n_{pig} excavation steps, the excavation of the gallery is initiated starting from the longitudinal tunnel wall. Referring to the notation of Fig. 11, L_{pg} is the considered step length for the gallery excavation, V_{pg} is the speed of the gallery excavation, and d_{0g} is the unlined length of the gallery. Each gallery excavation step is associated with time interval $t_{pg} = V_{pg}/L_{pg}$. After the gallery excavation is completed, we proceed to further excavation steps of the longitudinal tunnel.

For the sake of clearness, the main parameters defining the geometry domain as well as and excavation process and lining installation are summarized in Table 1.

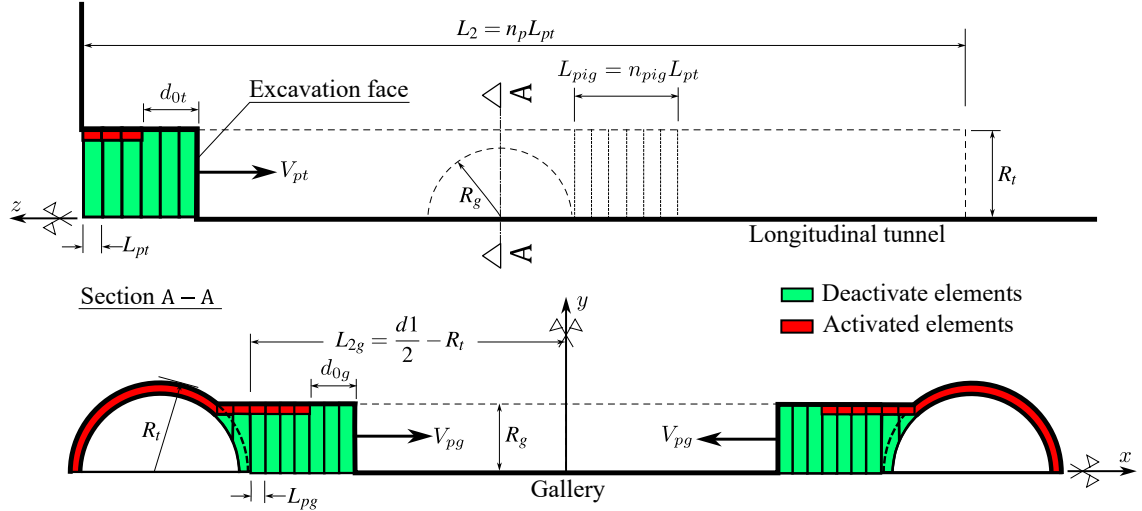


Figure 11: Schematic representation of the excavation process.

Table 1

Parameters related to the geometry of the domain, excavation and installation of the lining.

PARAMETERS	SYMBOL	UNIT	VALUES
Longitudinal tunnels			
Radius of the longitudinal tunnel	R_t	m	R_t
Thickness of the lining	e_t	m	$0.1R_t$
Step length of the excavation process	L_{pt}	m	$1/3R_t$
Unlined length	d_{0t}	m	$2L_{pt}$
Speed of the excavation face	V_{pt}	m/day	12.5
Excavation step time	t_p	day	L_{pt}/V_{pt}
Gallery			
Radius of the gallery	R_g	m	$2/3R_t$
Thickness of the concrete lining	e_g	m	$0.1R_t$
Step length of the excavation process ¹	L_{pg}	m	$1/3R_g$
Unlined length	d_{0g}	m	$2L_{pg}$
Speed of the excavation face	V_{pg}	m/day	12.5
Number of steps that starts gallery excavation	n_{pig}	un	15
Rest of domain			
Distance between longitudinal tunnel axes	d_1	m	$4R_t, 8R_t, 16R_t$
Thickness along vertical direction e_y	d_3	m	$20R_t$
Length of the unexcavated region	L_1	m	$10R_t$
Total excavated length	L_2	m	$100L_{pt}$
Thickness along transversal direction e_x	L_3	m	$20R_t + d_1/2$

¹Value of L_{pg} is slightly different for the last excavation step to match the gallery length.

During the tunnel construction phases, the time increment used for the time-dependent analysis is automatically managed by the ANSYS solver. The latter makes use of a semi-implicit scheme for the viscoplasticity solution, together with an automatic time stepping algorithm [38] in which the time step is defined as a fraction of time t_p for the phases of longitudinal tunnel excavation and as a fraction of t_{pg} for the phases of transverse gallery excavation. Furthermore, distinct time steps are considered for the time-dependent analysis during tunnelling process and post-excavation stage. After complete tunnel construction phases, the analysis is carried out for a period of about 3000 days to assess the time evolving deformation as well as long-term viscous effects on the final equilibrium of the tunnel structure. At that respect and in anticipation of the numerical results of the subsequent sections, the characteristic viscoplastic relaxation time [39] is equal to $\bar{\tau} = \eta f_0/E$, which is close to 30 days for model data of Table 2.

6. Preliminary numerical simulations and computational model verification

This section is aimed at applying the computational modeling to simulate deformation and stress in two academic twin tunnels configurations. The numerical results provided in these illustrative applications may be viewed as preliminary verifications of the F.E formulation. The first application refers to unlined twin tunnels excavated in an elastic rock mass, whereas the second application addresses the situation of unlined twin tunnels excavated in an elastoplastic medium.

6.1. Unlined twin tunnels in elastic medium

In the context of plane strain conditions, Guo et al. [40] addressed the configuration of deep twin tunnels excavated in a homogeneous elastic medium in which prevails a hydrostatic initial stress distribution. The authors formulated approximate analytical solutions for the stress distribution establishing far behind the face, which are induced in the rock mass by the excavation of two parallel circular tunnels. The model geometry of the twin circular tunnels as well as loading associated with initial hydrostatic stress (i.e., $\sigma_h = \sigma_v$) are displayed in Fig. 12.

Simulation of the problem has been addressed by means of the 3D finite element model and the numerical results obtained for the stress distribution far behind the faces of the twin tunnel shall be compared to the analytical stress solution derived by Guo et al. [40] in the framework of plane strain conditions. The simulations have been performed taking advantage of symmetry with respect to the midplane between twin tunnels and considering the following model data: tunnel radius $R_t = 4$ m, rock Young modulus $E = 500$ MPa and Poisson ratio $\nu = 0.23$, isotropic initial stresses of $\sigma_v = \sigma_h = 2.2$ MPa.

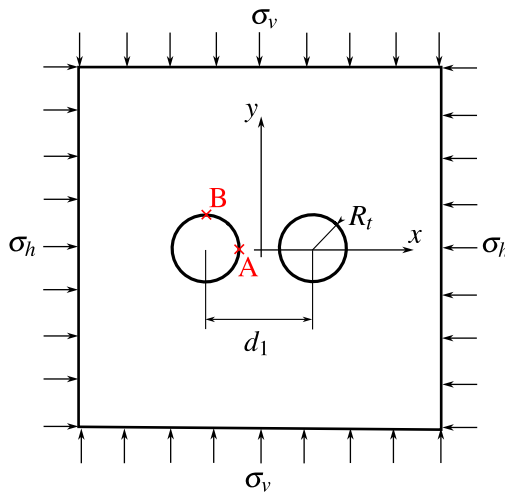


Figure 12: Geometry model and loading mode of the twin circular tunnels studied in Guo et al. [40].

Denoting by u_y the displacement component following the y -axis, Fig. 13 displays the convergence curves $U_B = -u_y(B)/R_t$ that characterize the inward movement at the tunnel roof $B(x = -d_1/2, y = R_t, z)$ as a function of normalized longitudinal distance to the tunnel face. Several values of normalized distances between the twin tunnels axes $d_1/2R_t$ have been investigated, and the configuration of single tunnel may be viewed as the limiting

case $d_1/2R_t \gg 1$. It is recalled that in the latter configuration, the convergence far from the tunnel face that is obtained from an elastic analysis reads $U = \sigma_v(1 + \nu)/E$. As expected, this figure indicates that the closer the longitudinal tunnels, the greater the convergence at the roof.

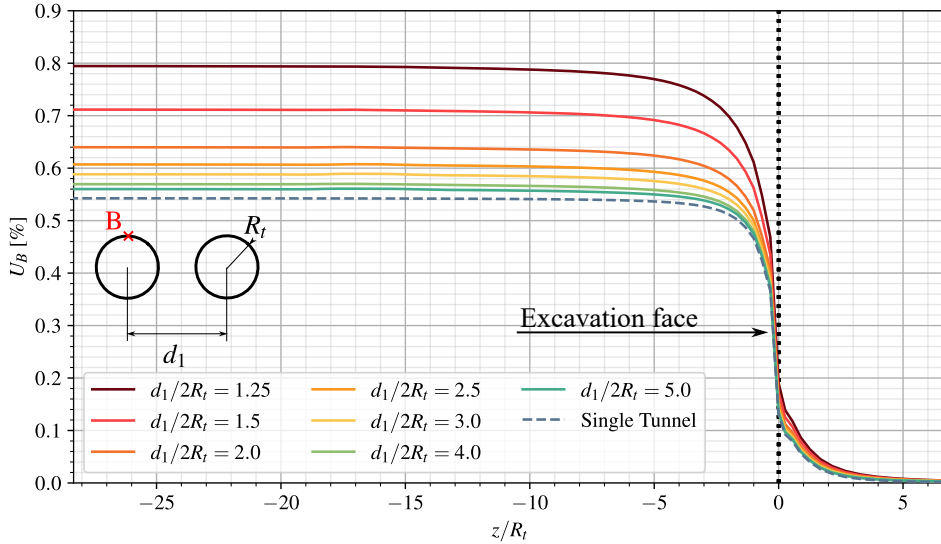


Figure 13: Convergence profiles at the tunnel roof (point B).

The tunnel deformation anisotropy induced by the twin tunnels proximity is illustrated in Fig. 14, which plots the ratio $U_B/U_A = u_y(B)/u_x(A)$ between the vertical displacement u_y at the roof B and the horizontal displacement u_x at the side wall A ($x = -d_1/2 + R_t, y = 0, z$). The results shown in this figure refer to a tunnel section located far behind the face at normalized distance $z/R_t = -25$. They emphasize the significative tunnel ovalization induced by the proximity of twin tunnel as the distance $d_1/2R_t$ decreases.

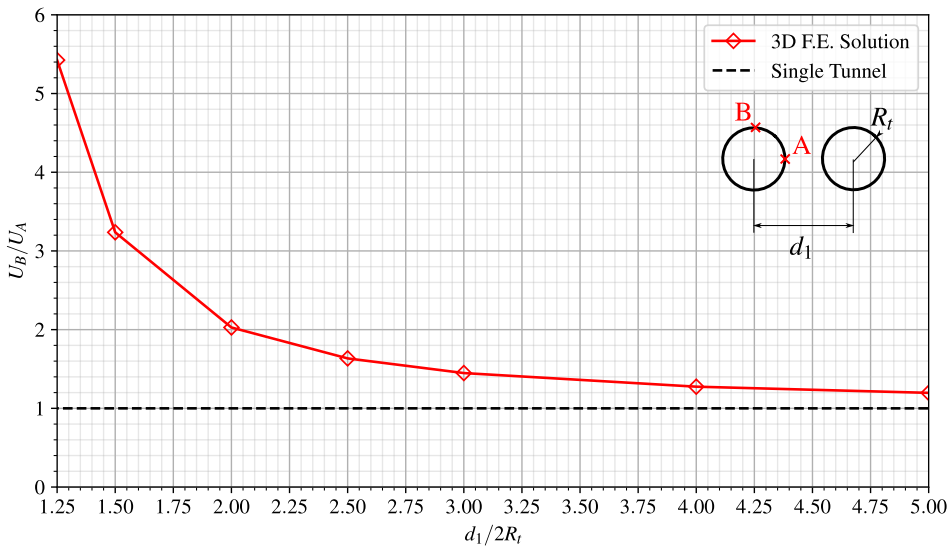


Figure 14: Illustration of the tunnel wall deformation anisotropy induced by twin tunnels proximity.

The stress distribution prevailing far from the tunnel face that were obtained from the 3D numerical simulations are compared in Fig. 15 to the stress solutions derived analytically and numerically in Guo et al. [40]. In this figure, the tangential stress concentration factor σ_{yy}/σ_v computed at the side wall A is plotted for several values of the normalized twin tunnels distance. The results of the theoretical solution to a plate containing two circular holes of equal size presented in Ling et al. [41] are also reported in Fig. 15. It is observed that the results of the 3D finite element simulations correspond to a tunnel section located at normalized distance $z/R_t = -25$ from the face, which is considered sufficient for the plane strain conditions to establish. Interestingly, the tangential stress concentration obtained for a deep single tunnel under plane strain condition simply reads $\sigma_{yy}/\sigma_v = 2$. Although the overall agreement observed between the different predictions, it appears from the comparison that the approximate analytical stress solution provided in [40] slightly overestimates the tangential stress computed at point A as the value of distance $d_1/2R_t$ increases.

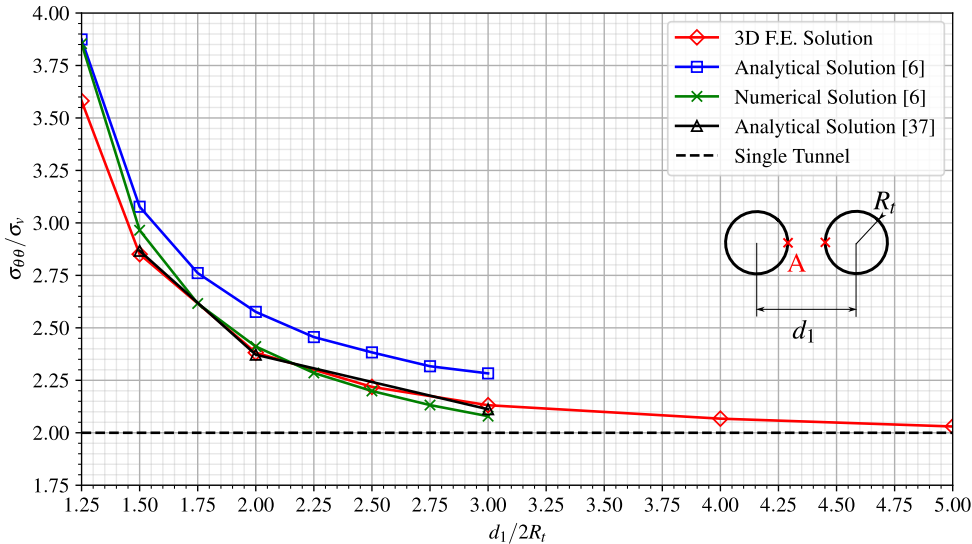


Figure 15: Tangential stress concentration factor at the side wall A versus twin tunnels distance $d_1/2R_t$.

Finally, Fig. 16 displays the distribution of tangential (orthoradial) stress $\sigma_{\theta\theta}$ around the tunnel boundary $\{r = R_t, 0 \leq \theta \leq \pi\}$ considering $d_1/2R_t = 1.5$. The predictions of stress component $\sigma_{\theta\theta}$ obtained from the 3D finite element simulations far behind the tunnel face are shown together with the strain plane solutions derived analytically in [40], emphasizing the ability of the computational model to accurately capture the effect of tunnels proximity on stress distribution.

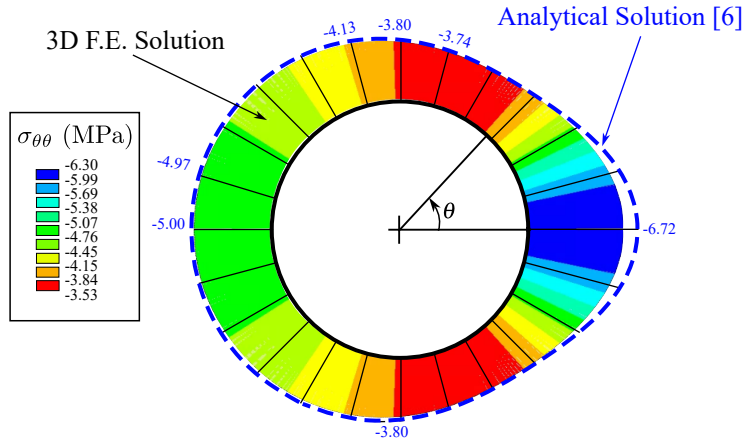


Figure 16: Distribution of tangential stress $\sigma_{\theta\theta}$ around the tunnel wall prevailing far behind the tunnel face (twin tunnels distance $d_1/2R_t = 1.5$).

Keeping in mind it addresses only an academic configuration, the results provided in this section may be viewed as a first preliminary verification of the accuracy of the computational model formulated for the mechanical interaction in deep twin tunnels.

6.2. Unlined twin tunnels in elastoplastic medium

In the analysis developed by Ma et al. [42], an approximate analytical solution has been formulated for the stresses and the plastic zone boundary around deep twin circular tunnels excavated in a homogeneous elastoplastic medium. The approach carried out under the assumption of plane strain condition makes use of the conformal transformation in the complex variable method to transform the solution of the elastic-plastic interfaces into the determination of the mapping function coefficients.

The geometry model and boundary loading conditions associated with the initial stress state are the same as depicted Fig. 12. Unlike the configuration studied in the preceding section, anisotropic initial stress distributions defined by $\sigma_h \neq \sigma_v$ shall be considered in the present analysis. As regards the rock constitutive model, an elastic-perfectly plastic behavior defined by a Mohr-Coulomb criterion with associated plastic flow rule has been adopted in the study. Furthermore, the formulation of stress solution for twin tunnels configuration was based on the premise that the plastic zone around each tunnel completely encloses the tunnel edge and the two plastic zones are not connected.

For the comparison purposes, numerical simulations are carried out by means of the 3D finite element model with the aim to investigate the effect of twin tunnels proximity on the tunnel wall deformation. The following model data has been considered in the F.E. simulations: tunnel radius $R_t = 1$ m, rock Young modulus $E = 20$ GPa, Poisson ratio $\nu = 0.3$, friction angle $\phi = 30^\circ$, cohesion $c = 5$ MPa or 2.5 MPa, initial vertical stress $\sigma_v = 30$ MPa or 40 MPa, initial horizontal stress $\sigma_h = 30$ MPa or 40 MPa. The simulation took advantage symmetry with respect to the midplane between the twin tunnels has been used for in the F.E. discretization model.

Similarly to the analysis developed in the preceding section, the convergence curves $U_B = -u_y(B)/R_t$, which reflects the inward movement at the tunnel roof $B(x = -d_1/2, y = R_t, z)$, is depicted in Fig. 17 as a function of normalized longitudinal distance to the tunnel face. Several values of normalized distances between the twin tunnels axes $d_1/2R_t$ have been investigated, together with the reference configuration of single tunnel, the latter being viewed as the limiting case $d_1/2R_t \gg 1$. As it could be expected from such simulations, this figure indicates that the proximity of tunnels significantly increases the convergence at the tunnel roof for small values, say $d_1/2R_t < 2$, of twin tunnel spacing. However, this effect rapidly become negligible as soon as the tunnel spacing increases.

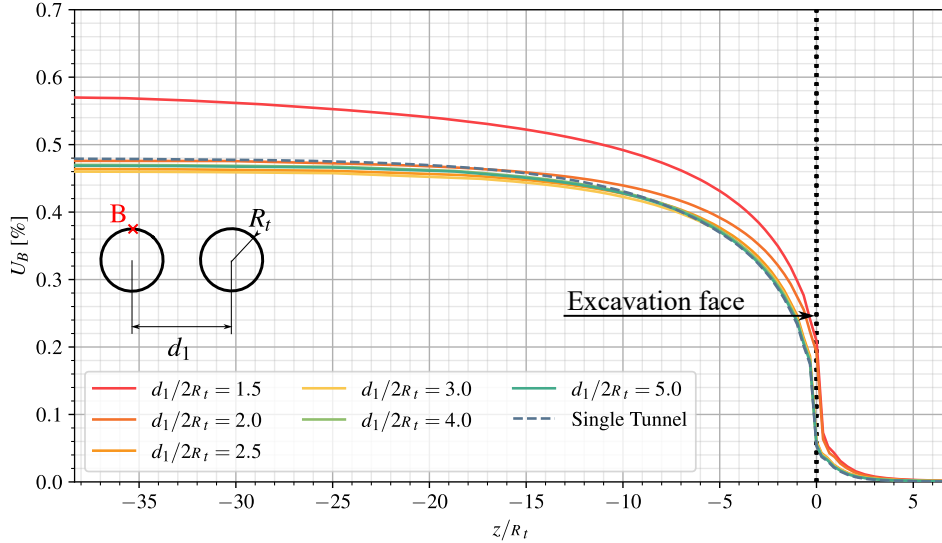


Figure 17: Convergence profiles at the tunnel roof (point B): $c = 5 \text{ MPa}$, $\sigma_v = \sigma_h = 30 \text{ MPa}$.

An important feature of the twin tunnels deformation is related to the anisotropy induced by the mutual interaction as the normalized tunnel spacing $d_1/2R_t$ decreases. In that respect, anisotropy of tunnel deformation is illustrated in Fig. 18, which presents the variations of the ratio $U_B/U_A = u_y(B)/u_x(A)$ between the vertical displacement u_y at the roof B and the horizontal displacement u_x at the side wall $A(x = -d_1/2 + R_t, y = 0, z)$ as a function of normalized twin tunnel spacing $d_1/2R_t$. These results refer to a tunnel section located far behind the face at normalized distance $z/R_t = -35$. As observed in the elastic case studied in the preceding section, the proximity of twin tunnels reflected by small values of normalized distance $d_1/2R_t$ is responsible for tunnel ovalization. The magnitude of horizontal displacement at the side wall A is actually larger in than that of vertical displacement at the tunnel roof B , thus indicating an ovalization in the vertical direction (i.e., parallel to y -axis).

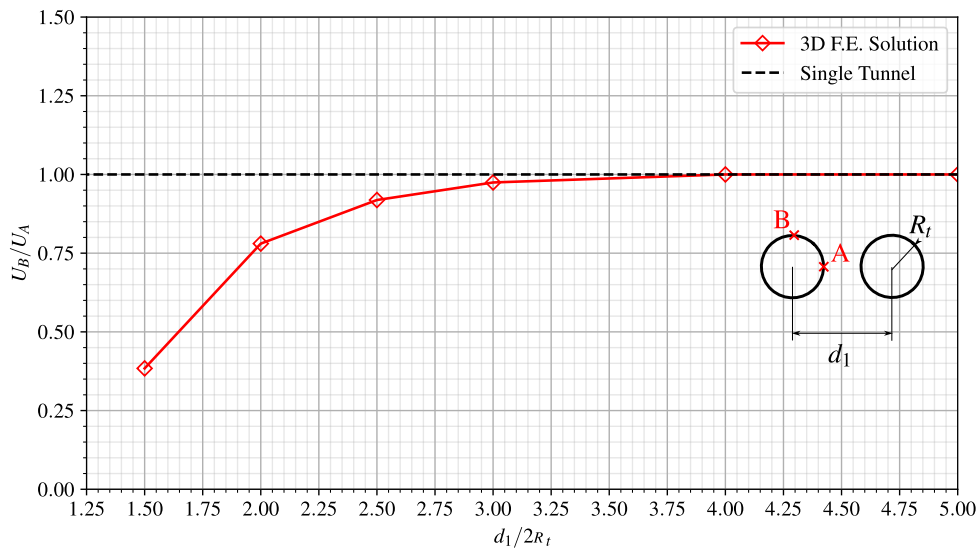


Figure 18: Tunnel wall deformation anisotropy induced by twin tunnels proximity: $c = 5 \text{ MPa}$, $\sigma_v = \sigma_h = 30 \text{ MPa}$.

The stress distribution prevailing far from the tunnel face that were obtained from the 3D numerical simulations are compared in the to the approximate stress solutions derived by Ma et al. [42] within the context of plane strain conditions. Fig. 19 displays such a comparison in terms of predicted plastic zone surrounding the twin tunnels considering a normalized tunnel spacing of $d_1/2R_t = 2.5$. Different values have been considered for rock cohesion c and initial stresses σ_v and σ_h . It appears from the latter figure that the finite element modeling produces predictions very similar to those provided in 19. The results also illustrate that larger plastic zones arise when the cohesion c is smaller.

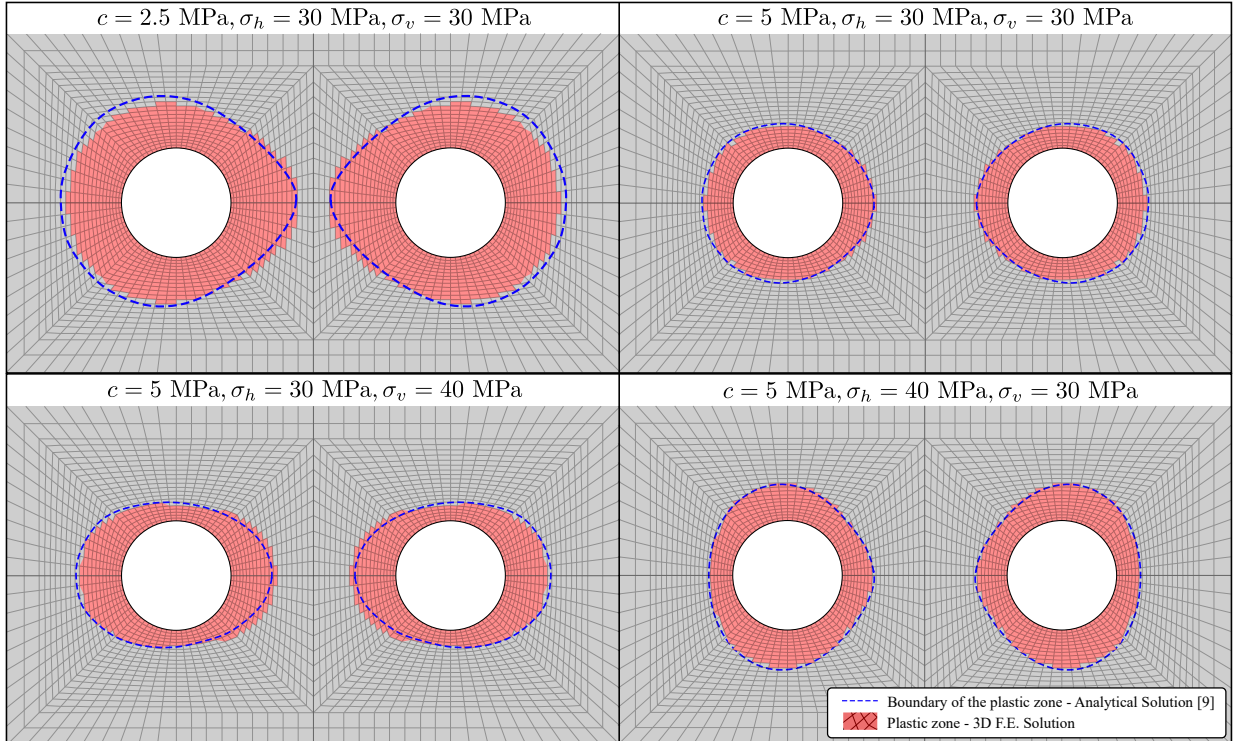


Figure 19: The plastic zone extent obtained from the present F.E. simulations and from the stress solution provided in [42].

Further comparisons are shown in Fig. 20, which presents the plots of radial σ_{rr} , and orthoradial $\sigma_{\theta\theta}$ stress components along three radial paths defined in polar coordinates by $\theta = 45^\circ, 90^\circ$ and 135° . It should be pointed out that, although the F.E. element simulations make use of the Drucker-Prager yield surface inscribed to the Mohr-Coulomb one (used in the solution of Ma et al. 42), the numerical predictions are matching well with the analytical stress solution.

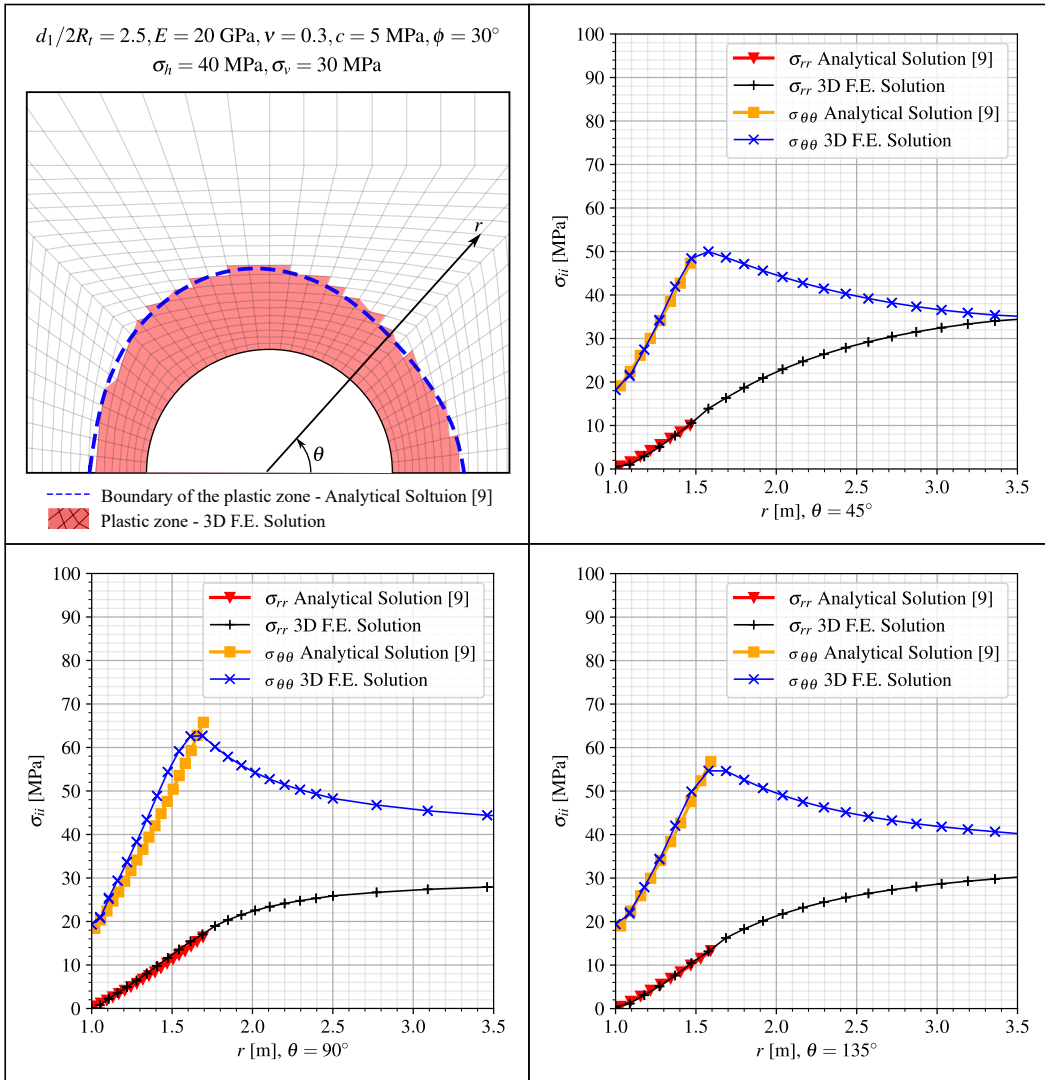


Figure 20: Distribution of radial and orthoradial stress components along different radial directions: comparison between numerical and analytical predictions.

7. Three-dimensional finite element simulations

This section provides some numerical results related to rock deformation in twin tunnels with transverse gallery obtained from the 3D computational model presented in sections 3, 4 and 5. It is emphasized that the primary objective herein is to illustrate the capabilities of the proposed formulation to address within a 3D context the configuration of a complex tunnel structure involving nonlinear and time-dependent couplings. Elaboration of an exhaustive parametric analysis integrating the effects of geometrical, constitutive and loading parameters is notably beyond the scope of the numerical application.

7.1. Model data and preliminary considerations

The rock constitutive data used in the subsequent analysis refer to a deep clay from eastern Paris basin (Aisne region, France) studied in [20, 22, 24, 43]. The material properties including elastoplastic and viscoplastic parameters summarized in Table 2 have been evaluated and calibrated from an extensive series of laboratory tests performed under undrained conditions [20, 24, 43]. The Aisne clay rocks exhibit high density (2.01 to 2.57 g/cm³), a low average water content (between 3 to 11%) and relatively low porosity (typically less than 20%). It is therefore assumed that

hydromechanical coupling can be neglected in the analysis of rock material deformation. In particular, the creep tests indicated that the long-term effects primarily stem from material viscosity, with a very low proportion induced by pore pressure redistribution. An important characteristic of the behavior such clay is that irreversible strains are observed in cyclic tests even at small values of axial strain (less than 0.3%). The instantaneous undrained triaxial tests performed at high confining pressure values, such as those prevailing in the rock mass at approximately 450 m deep, indicated that the maximum deviatoric stress remains approximately constant, thus suggesting a Tresca-type failure criterion for the short-term component of the behavior. As for the long-term behavior, the creep tests revealed that the deviatoric stress threshold beyond which the material exhibits creep deformation is almost independent on the mean stress, suggesting that the time-dependent behavior component can be conveniently described by a Tresca-like criterion. Comparison of instantaneous and delayed behaviors reveals that short-term cohesion exceeds long-term cohesion within a ratio ranging between 1.2 and 2. Based on these observations, the constitutive model data adopted for the elastoplastic and viscoplastic components of rock material behavior is summarized in Table 2.

Table 2 also presents the constitutive parameters used for the lining used for the twin tunnels and gallery, the instantaneous relaxation modulus under uniaxial stress at 28 days being referred to as $E_{c_{28}}$. In the analyses that considers elastic behavior of the lining, the concrete elastic modulus is set equal to $E_{c_{28}}$. When viscoelastic behavior is adopted for the lining, the relaxation modulus evolves in time according to the Generalized Kelvin model described in section 4, whereas the Poisson ratio is assumed to be constant within the time interval of analysis. During the tunnel construction process, loading and creep of each lining segment starts from the moment it is activated with properties at age $t_0 = 1$ day, whereas shrinkage effects are assumed to take part at the age of $t_s = 7$ days.

Table 2

Constitutive parameters used in the numerical analysis.

PARAMETERS	SYMBOL	UNIT	VALUES
Constitutive model of rock mass			
Young's modulus	E	MPa	1500
Poisson's ratio	ν	-	0.49
Plastic cohesion	c	MPa	$4\sqrt{3}/2$
Plastic friction angle	ϕ	°	0
Viscoplastic cohesion	c_{vp}	MPa	$2\sqrt{3}/2$
Viscoplastic friction angle	ϕ_{vp}	°	0
Power law parameter	n	-	1
Reference parameter	f_0	MPa	1
Viscosity coefficient	η	day	40000
Constitutive model of lining			
Characteristic compressive strength at age of 28 days	f_{ck}	MPa	20
Modulus of elasticity at the age of 28 days	E_{c28}	MPa	30303
Poisson's ratio	ν_c	-	0.2
Coefficient defining instantaneous relaxation modulus [31]	s	-	0.2
Relative humidity of ambient environment	RH	%	70
Notional size of member - longitudinal concrete lining	h_t	cm	0.2111
Notional size of member - gallery concrete lining	h_g	cm	0.2176
Age of concrete at the beginning of shrinkage	t_s	days	7
Shrinkage coefficient depending on cement type [31]	β_{sc}	-	8
Temperature	T	°C	20
Age of concrete at loading	t_0	days	1

The parameters defining the structure geometry as well as the excavation and lining installation process are provided in Table 1. All the length parameters are normalized by the tunnel radius R_t , which amounts to formally consider radius $R_t = 1$ m in the numerical simulations. As mentioned in Table 1, three different values shall be considered in the simulations for the distance between twin tunnels axes, namely $d_1 = 4R_t$, $d_1 = 8R_t$, and $d_1 = 16R_t$. In addition, constant values of tunnel and gallery advancement rates are considered and fixed to $V_{pt} = V_{pg} = 12.5$ m/day. As regards the initial stress state prevailing prior to excavation processes, hydrostatic stress distribution with $\sigma_v = \sigma_h = 9$ MPa, corresponding to geostatic conditions at depths of about of 450 m, is adopted in the subsequent simulations.

The numerical study investigates the long-term and short-term tunnel convergence profiles considering various constitutive models for the rock mass (elastic, elastoplastic, viscoplastic or elastoplastic-viscoplastic) and for the lining (elastic and viscoelastic). For the comparison purposes, the configuration of unlined tunnel as well as the configurations with or without transverse gallery will also be analyzed. To facilitate the description of the different configurations addressed below, Table 3 provides the list of each configuration as well as associated abbreviation used to refer to in the presentation of numerical results.

Table 3

Configurations and associated abbreviations used in numerical simulations.

DESCRIPTION	ABBREVIATION
Elastic rock mass	E
Elastoplastic rock mass	EP
Elastoviscoplastic rock mass	VP
Elastoplastic-Viscoplastic rock mass	EPVP
No lining	NL
Elastic lining	EL
Viscoelastic lining	VEL
Long-term	LT
End of excavation process (Short-term)	ST
With Gallery	WG
No Gallery	NG

Denoting by u_y the displacement component along the vertical y -axis, all the results presented in the following analyses will specifically refer the convergence profile $U_B = -u_y(B)/R_t$ that characterizes the inward movement of the tunnel roof $B(x = -d_1/2, y = R_t, z)$ as a function of the normalized algebraic longitudinal distance z/R_t from the excavation face. In addition, point $C(x = -d_1/2, y = R_t, z = -25R_t)$ has been chosen as representative of the equilibrium convergence U_C far behind the tunnel face and transverse gallery. When the gallery intersects the longitudinal tunnel, the highest convergence value U_{peak} highlighted in the plots of convergence curves refers to point $D(x = -d_1/2, y = R_t, z = L_1 + L_2/2)$ located at the roof of longitudinal tunnel section lying at the tunnel/transverse gallery junction.

The first feature of tunnel deformation to be mentioned is related to the tunnel deformation anisotropy (or ovalization) induced by the twin tunnels proximity. A single circular tunnel excavated in a homogeneous isotropic rock mass with hydrostatic initial stress state will deform symmetrically so that the circular shape of tunnel wall will be preserved throughout the excavation process. As already pointed out in the preliminary numerical simulations presented in section 6, the mutual interaction associated with twin tunnels proximity will in contrast result in anisotropic deformation of the tunnel wall, the ovalization effect being more pronounced as the distance between twin tunnels axes d_1 decreases. For illustrative purposes, Fig. 21 presents schematic plots of the deformed tunnel wall far behind the face together with trajectory of monitoring point B considering three different values of normalized twin tunnel spacing d_1/R_t . The configuration shown in this figure corresponds to elastoplastic rock mass (EP), elastic lining (EL) and transverse gallery (WG). It should be however kept in mind that due to tunnel ovalization, U_B would not be therefore sufficient for characterizing the whole deformation of the tunnel wall.

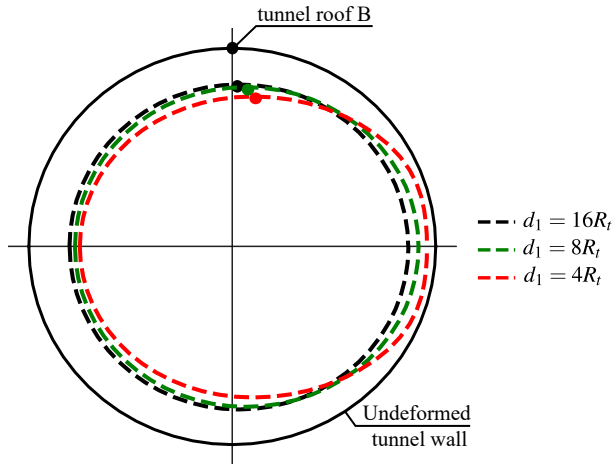


Figure 21: Illustration of the deformation anisotropy induced by twin tunnels proximity.

The second feature of the tunnel deformation that deserves to be mentioned refer the specific deformation patterns prevailing in the region surrounding the tunnel wall. In consistence with experimental data, the plastic cohesion c and viscoplastic cohesion c_{vp} reported in Table 2 comply with condition $c > c_{vp}$. This notably implies that irreversible viscoplastic strains will be activated earlier as the tunnel excavation. Schematic representation of deformation patterns within the rock mass is illustrated in Fig. 22.

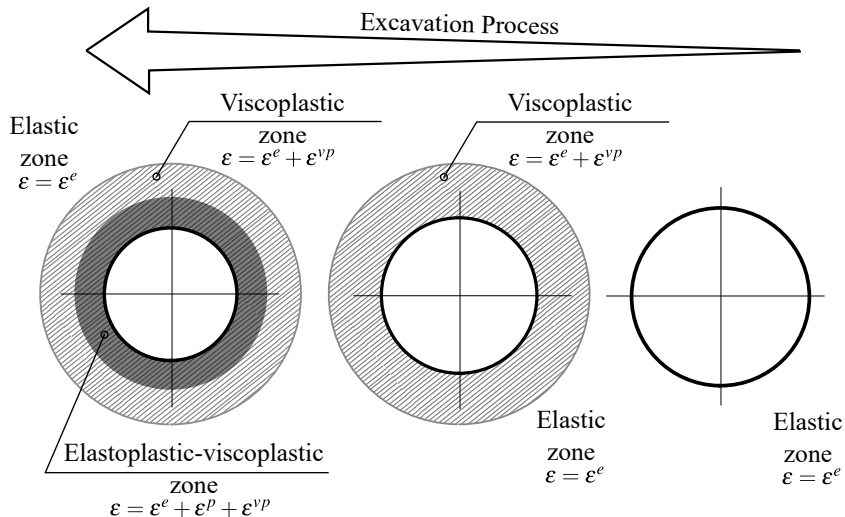


Figure 22: Evolution of deformation zones as the tunnel excavation proceeds.

[parei aqui]

7.2. Short and long-term convergence profiles

Figs. 23, 24, and 25 show the convergence profiles in the twin tunnels with gallery (WG) considering the different constitutive models of the rock mass (E - blue, EP - yellow, VP - magenta, EPVP - red and green) and of the lining (EL and VEL). The interaction effect rising from twin tunnels proximity is investigated by considering three values $d_1 = 4R_t$, $d_1 = 8R_t$, and $d_1 = 16R_t$. The solid lines refer to short-term analysis (ST) whereas the dashed lines to long-term analysis (LT).

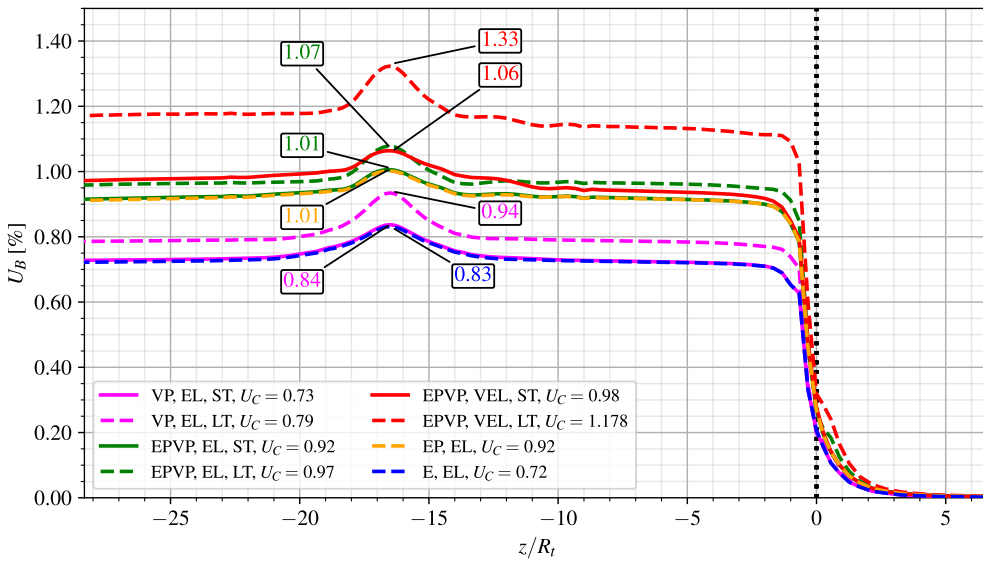


Figure 23: Convergence Profiles: short-term (ST) and long-term (LT) analyses for the configuration with gallery (WG) and distance between twin tunnels $d_1 = 16R_t$.

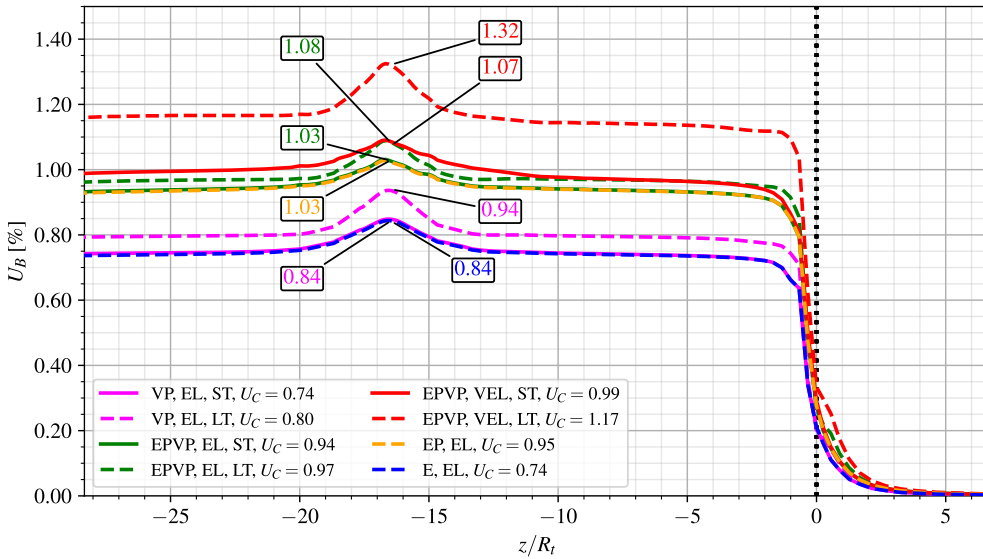


Figure 24: Convergence Profiles: short-term (ST) and long-term (LT) analyses for the configuration with gallery (WG) and distance between twin tunnels $d_1 = 8R_t$.

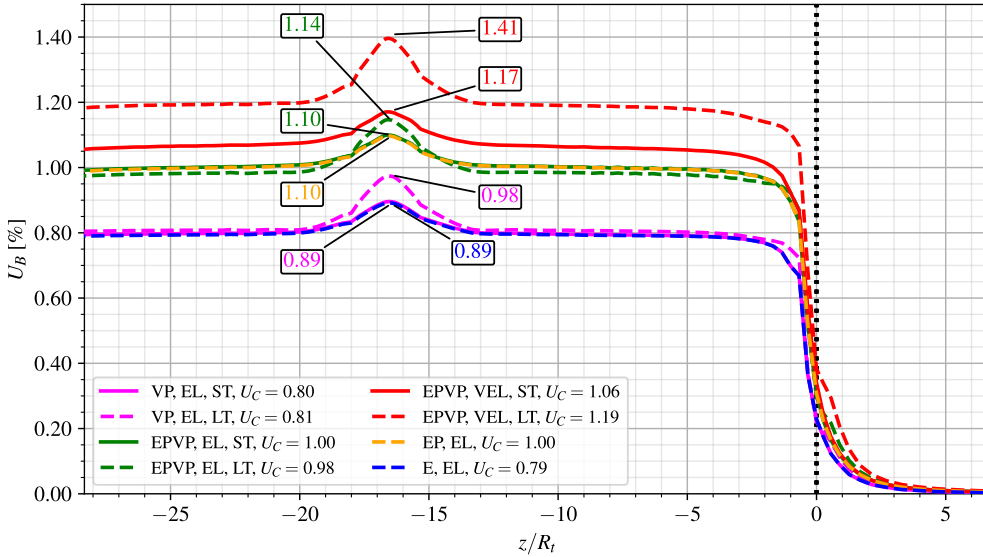


Figure 25: Convergence Profiles: short-term (ST) and long-term (LT) analyses for the configuration with gallery (WG) and distance between twin tunnels $d_1 = 4R_t$.

For all investigated values of twin tunnels distance d_1 , the convergence profiles obtained in short-term (ST) analyses are very similar for both the E-EL (blue dashed line) and the VP-EL (magenta solid line) constitutive model configurations. This mainly attributed to relatively high value considered for the tunnel/gallery advancement rate and lining installation (excavation speed $V_{pt} = V_{pg}$), thus limiting the viscous effects on the tunnel deformation. The same explanation holds regarding the results derived from the short-term (ST) analyses with the EP-EL (yellow dashed line) or EPVP-EL (green solid line) constitutive model configurations. However, the viscous effects give rise to delayed tunnel deformation progressively affecting the long-term (LT) convergence (dashed green line) at the tunnel roof B. The discrepancy between short-term and long-term responses is more pronounced when a time-dependent viscoelastic lining is considered, as clearly indicated from the convergence associated with the EPVP-VEL model (solid and dashed red lines).

It is noted that the relatively high stiffness considered of the elastic lining is likely to significantly reduces the viscous component of tunnel wall deformation. This can be illustrated by analyzing the short-term and long-term convergences for VP-EL model (solid and dashed magenta line). In this configuration, the twin tunnels proximity induces a substantial increase in the short-term (ST) prediction of U_C when comparing $d_1 = 8R_t$ and $d_1 = 4R_t$, whereas the long-term (LT) convergence hardly changes mainly due to the restriction imposed by the stiff lining.

Referring to the configuration analyzed in Figs. 23, 24, and 25, the ovalization effect may be illustrated by visualizing in Fig. 26 the anisotropic deformation of a tunnel cross-section located far behind the face in the particular case of twin tunnel distance $d_1 = 4R_t$. In this figure, the configuration of a single circular tunnel ($d_1 \rightarrow \infty$) is also shown as a reference case.

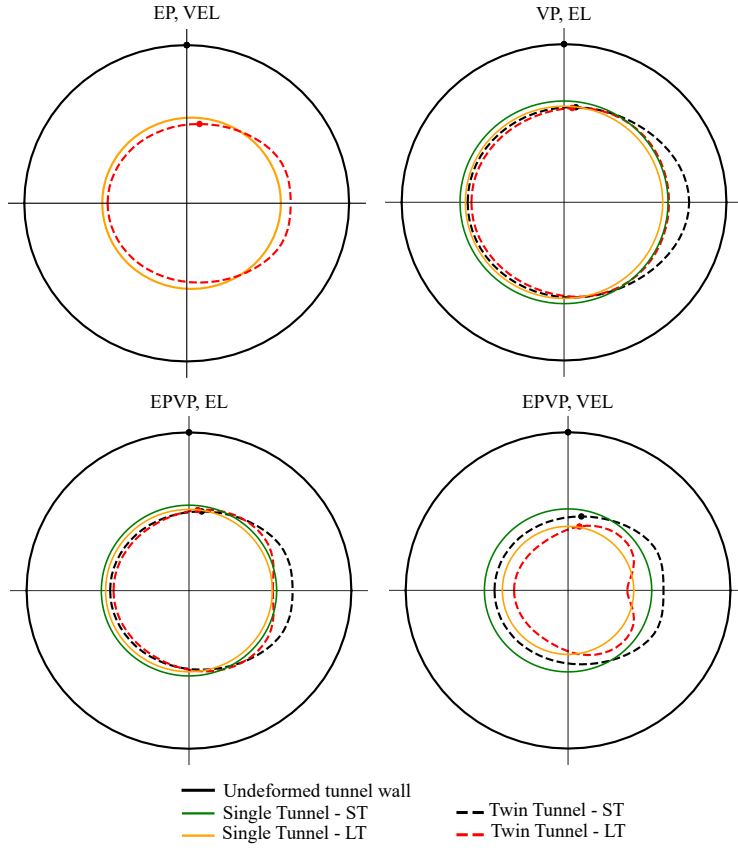


Figure 26: Illustration of deformation anisotropy induced: configuration with gallery (WG) and distance between twin tunnels $d_1 = 4R_t$.

In that respect, Fig. 27 provides further illustration of the ovalization effect by plotting the anisotropy ratio $U_B/U_A = u_y(B)/u_x(A)$ between the vertical displacement u_y at the roof B and the horizontal displacement u_x at the side wall A ($x = R_t - d_1/2, y = 0, z$). The results presented in this figure correspond to twin tunnels without transverse gallery (NG) and distance $d_1 = 4R_t$. The results suggest a more pronounced ovalization effect short-term tunnel deformation (solid lines).

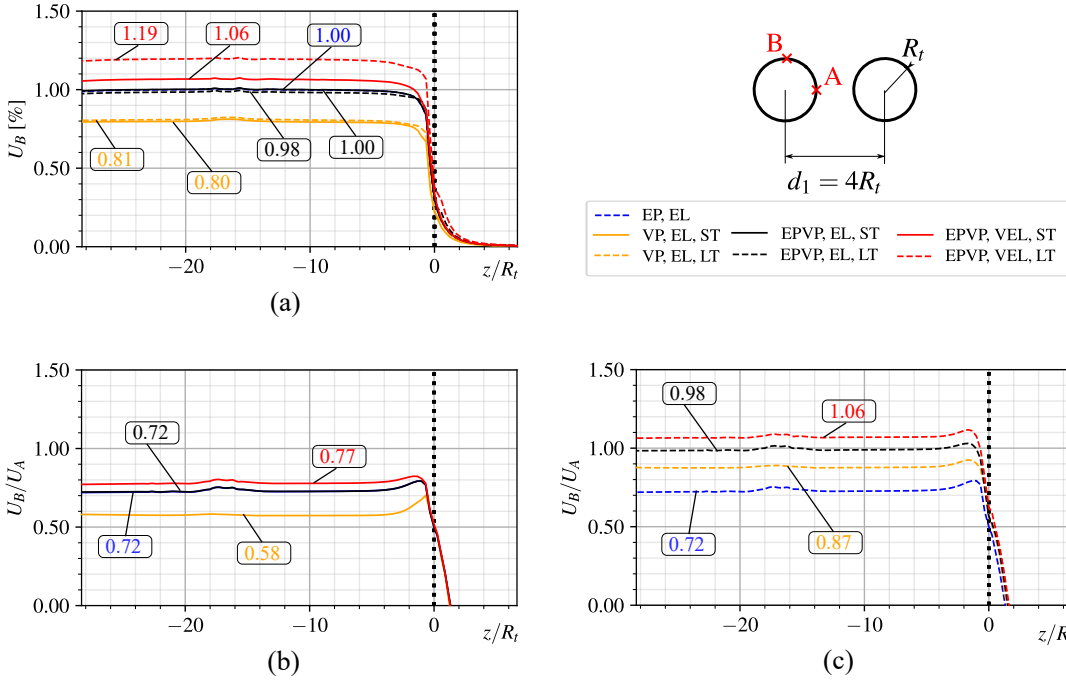


Figure 27: Deformation anisotropy induced by twin tunnels proximity for the configuration without gallery (NG) and distance between twin tunnels $d_1 = 4R_t$: (a) convergence profile at the tunnel roof B, (b) anisotropy ratio obtained in short-term analysis, (c) anisotropy ratio obtained in long-term analysis.

7.3. Additional numerical analysis: impact of creep deformation

This section provides further numerical results obtained from long-term and short-term analyses, with particular emphasis on the effect of time-dependent behavior of the rock material and lining constituent materials. Fig. 28 displays the long-term convergence profiles for $d_1 = 16R_t$, $8R_t$ and $4R_t$ (yellow, green and red lines, respectively) considering viscous constitutive models: viscoplastic rock mass with elastic lining (VP-EL - solid lines), elastoplastic-viscoplastic rock mass with elastic lining (EPVP-EL - dashed line) and viscoelastic lining (EPVP-VEL - dotted lines). To emphasize the interaction rising from twin tunnels proximity and transverse gallery, the results obtained in the reference configuration of a single tunnel (black lines) are also shown. Close values of the peak convergence U_{peak} are obtained at the tunnel roof for the EPVP-VEL model with $d_1 = 16R_t$ (yellow dotted line) and with $d_1 = 8R_t$ (green dotted line). This result may be explained by the fact the overall interaction effect on tunnel convergence results from the competing effects of twin tunnel proximity (defined by d_1) and the time necessary for complete gallery excavation and its intersection with longitudinal tunnel (also defined by length by d_1). The results indicated that these competing phenomena lead to equivalent overall effect in the cases of $d_1 = 8R_t$ and $d_1 = 16R_t$. In the case of $d_1 = 4R_t$ (red dotted line), the effect of twin tunnel proximity appears to be predominant, which lead to higher value of the peak convergence U_{peak} .

Referring to EPVP-VEL and EPVP-EL models (dotted lines and dashed lines), it can be seen from the results of Fig. 28 that higher convergence values are associated with time-dependent behavior of the lining. Unlike the stiff elastic lining, the aging viscoelastic lining induces evolving tunnel convergence along the excavation process.

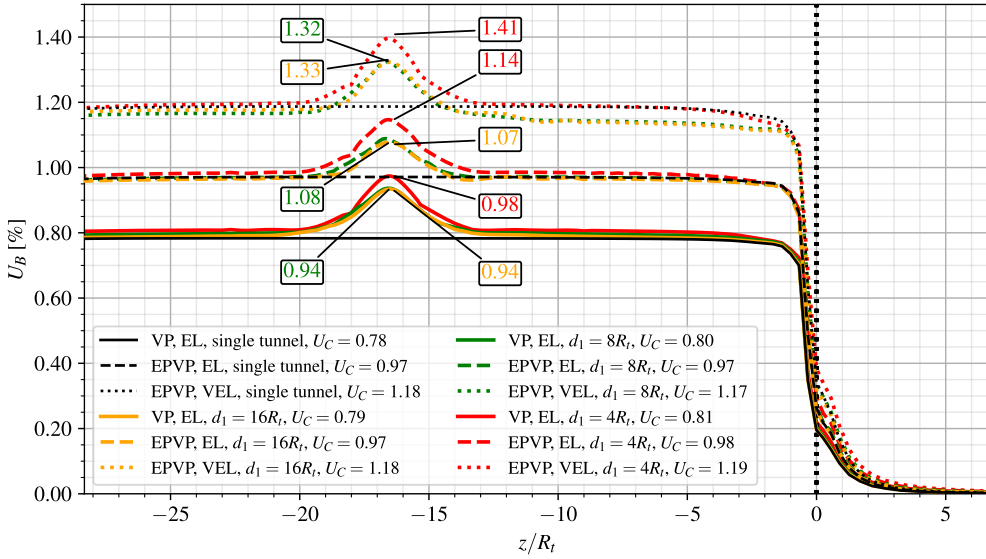


Figure 28: Long-term convergence profiles for the configuration of twin tunnels with transverse gallery (WG): effect of rock mass and lining creep deformation.

The impact of creep deformation on the tunnel convergence can alternatively be illustrated based on the comparison of the numerical predictions obtained in the cases of instantaneous behavior (elastoplastic, elastic) and time-dependent behavior (viscoplastic, viscoelastic) for the constituent materials. Fig. 29 depicts the convergence profiles obtained for $d_1 = 16R_t$, $8R_t$ and $4R_t$ (yellow, green and red lines, respectively) considering the configurations of elastoplastic rock mass with elastic lining (EP-EL - solid lines), elastoplastic-viscoplastic rock mass with viscoelastic lining in short-term analysis (EPVP-VEL-ST - dotted lines) and elastoplastic-viscoplastic rock mass with viscoelastic lining in long-term analysis (EPVP-VEL-LT - dashed lines). The case of single circular tunnel ($d_1 \rightarrow \infty$) is also analyzed as reference configuration (black lines).

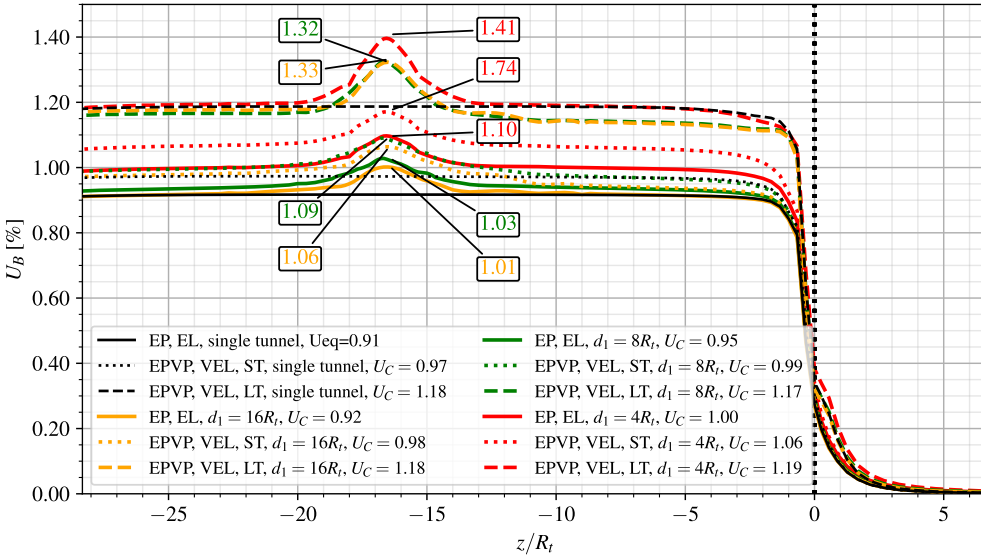


Figure 29: Short-term and long-term convergence profiles obtained for the configuration of twin tunnels with transverse gallery (WG): instantaneous versus delayed behaviors of the rock and lining constituent material.

Once again, the result predictions shown in this figure emphasize the significative impact of the viscoelastic lining behavior on the short-term convergence profile of the tunnels. At short-term (ST), the elastoplastic-viscoplastic rock mass with viscoelastic lining (EPVP-VEL - dotted lines) leads to higher convergences when compared to the elastoplastic rock mass with elastic lining (EP-EL - solid lines). This is mainly attributed to the fact the early age viscoelastic lining (VEL) exhibits lower relaxation modulus than the stiffness E_{c28} considered for elastic lining (EL), thus resulting in higher tunnel deformation. Regarding the long-term analysis (LT), even though the viscoelastic lining (VEL) (dashed lines) exhibit increasing relaxation modulus due to aging phenomenon, the creep deformation of both the rock and lining constituents result in significantly higher convergences at the tunnel roof when compared to obtained for elastoplastic rock with elastic lining (EP-EL - solid lines). A noticeable increase in the magnitude of U_{peak} , induced by the interaction with transverse gallery, is also observed from the short-term response (dotted lines) to the long-term response (dashed lines), highlighting once again the influence of the delayed behavior of the rock and the lining.

7.4. Effect of the lining stiffness on the tunnel convergence

In tunnel deformation analyses, the behavior of the concrete lining is classically characterized by the elastic stiffness parameter, which relates the normal stress exerted by the surrounding the rock mass and the normalized lining normal displacement (convergence). The elastic stiffness parameter is computed from the elastic properties of concrete material and the lining thickness (normalized by the tunnel radius) [44, 45]. This concept is extended herein to case of viscoelastic lining by introducing the instantaneous stiffness modulus at 28 days K_{c28} as:

$$K_{c28} = \frac{E_{c28}}{1 + v_c} \frac{1 - (1 - e_t/R_t)^2}{(1 - 2v_c) + (1 - e_t/R_t)^2} \quad (12)$$

In the above analyses of sections 7.1, 7.2 and 7.3 the lining thickness were fixed to $e_t = e_g = 0.1R_t$, corresponding to lining stiffness $K_{c28} = 3400$ MPa. As far as the tunnel deformation is concerned, the latter value characterizes a rather stiff lining, which might be a predominating factor for the control of tunnel convergence.

To assess the effect of the lining stiffness on the convergence profile, a smaller value $e_t = e_g = 0.03R_t$, corresponding to lining stiffness modulus $K_{c28} = 970$ MPa, will be in the numerical simulations. Referring to the particular case of a rock mass exhibiting elastoplastic behavior (EP), that is only instantaneous behavior, Fig. 30 and

Fig. 31 display the convergence profiles at tunnel roof predicted respectively for $d_1 = 16R_t$ and $d_1 = 4R_t$. Three configurations for the support lining are considered: unlined structure (NL - dashed lines), elastic lining with lower stiffness $K_{c28} = 970$ - dotted lines), and elastic lining with higher stiffness $K_{c28} = 3400$ - solid lines). In addition, the numerical simulations include the cases with transverse gallery (WG - blue lines) and without gallery (NG - yellow lines). The reference configuration of a single tunnel is also studied (black lines).

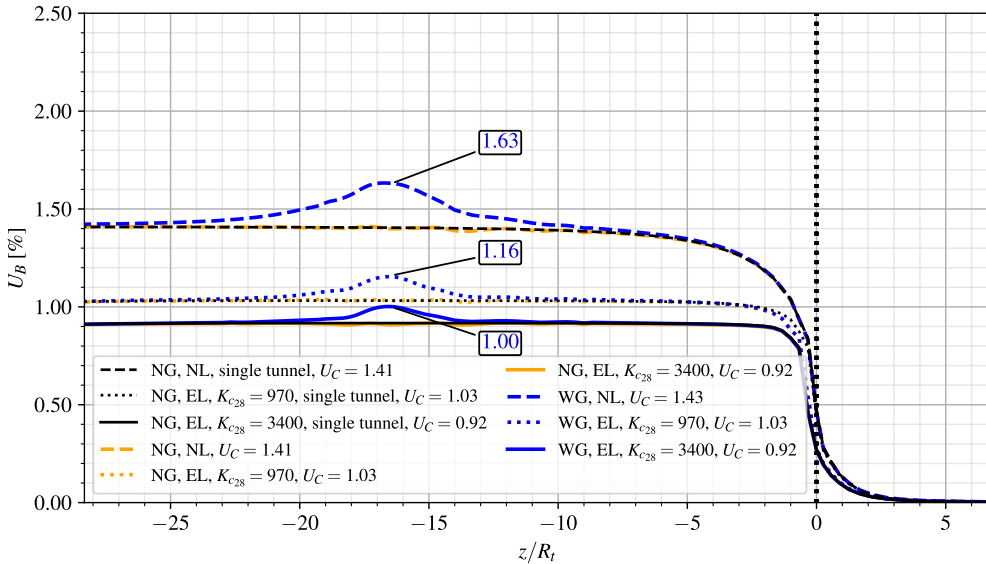


Figure 30: Effect of lining stiffness on the convergence profiles for the configuration of twin tunnels with and without transverse gallery and distance between twin tunnels $d_1 = 16R_t$ - elastoplastic rock mass, without and with elastic lining.

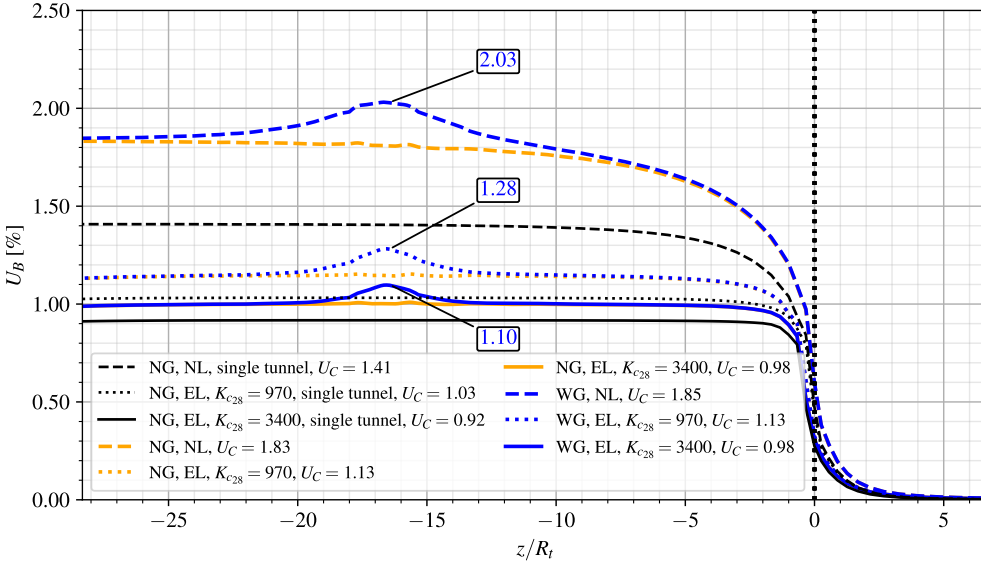


Figure 31: Effect of lining stiffness on the convergence profiles for the configuration of twin tunnels with and without transverse gallery and distance between twin tunnels $d_1 = 4R_t$ - elastoplastic rock mass, without and with elastic lining.

As observed in the simulations of preceding sections, the equilibrium convergence U_C far behind the tunnel face is almost unaffected by the presence of transverse gallery.

Regarding first the effect of lining stiffness on the convergence of single tunnel, the stiffer lining (black solid line) leads to a stabilized convergence reduction of approximately 35% with respect to unlined structure (black dashed line), whereas this reduction is only 12% for the moderate stiffness lining (black dotted line).

For twin tunnels with spacing $d_1 = 16R_t$, the predictions of stabilized convergence U_C (blue and yellow lines) provided in Fig. 30 are close for each lining configuration to those obtained for a single tunnel (black lines). In contrast, the interaction between the twin tunnels reveals significative when the spacing reduces to $d_1 = 4R_t$. In that case, the combined impact of lining support and twin tunnels proximity can be assessed by comparing in Fig. 31 the values of convergence U_C predicted for $d_1 = 4R_t$ (yellow and blue solid lines) and $d_1 \rightarrow \infty$ (single tunnel - black lines). Compared to the convergence of single tunnel, the increase in convergence induced by twin tunnels proximity reaches values of 30% for unlined structure, 10% for the moderate stiffness lining and 6.5% for the higher stiffness stiff.

Analyzing the effect of lining stiffness on the disturbed region associated along the convergence profile with the presence of transverse gallery, it is first observed that the increase in stiffness reduces in all studied configurations the extent of the disturbed region, whereas the twin tunnels spacing has little impact. For the configuration of spacing $d_1 = 16R_t$, where the interaction due to twin tunnels proximity is expected to be minor, the ratio $(U_{peak} - U_C)/(U_C)$ defining the relative variation between peak value and stabilized tunnel roof convergence is about 14%, 12.5% and 8.7% according to the lining stiffness value: $K_{c28} = 0$ (unlined), $K_{c28} = 970$ MPa and $K_{c28} = 3400$ MPa. The values of this ratio are altered to about 9.7%, 13% and 12% for the configuration with spacing $d_1 = 4R_t$ in which both effects of lining stiffness and tunnels proximity are simultaneously acting.

In line with the previous analysis investigating the impact of instantaneous stiffness modulus K_{c28} of the lining, Fig. 32 and Fig. 33 present the long-term convergence results in the configurations of elastoplastic-viscoplastic rock mass (EPVP) and viscoelastic lining (VEL) with gallery (WG - blue lines) and without gallery (NG - yellow lines), considering twin tunnels spacing $d_1 = 16R_t$ and $4R_t$, respectively. The results obtained for the reference single tunnel configuration are also provided (black lines).

Similar to the previous analysis involving constituent materials that exhibit only instantaneous behaviors, the results Fig. 32 indicate that the predictions of stabilized convergence U_C in the case of twin tunnels with spacing $d_1 = 16R_t$ are very close to obtained for single tunnel.

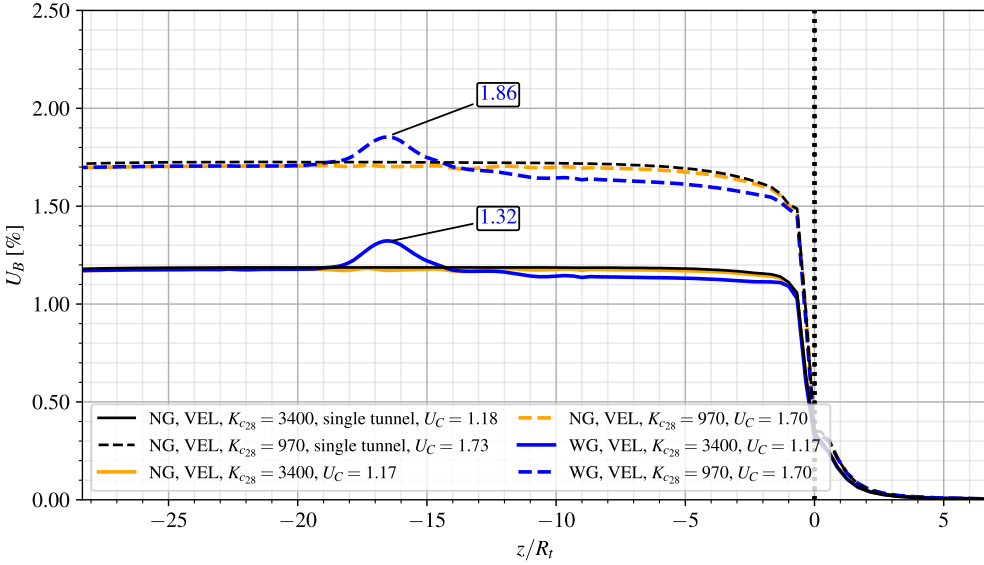


Figure 32: Effect of instantaneous lining stiffness on the long-term convergence profiles for the configuration of twin tunnels with and without transverse gallery and distance between twin tunnels $d_1 = 16R_t$ - elastoplastic-viscoplastic rock mass with viscoelastic lining.

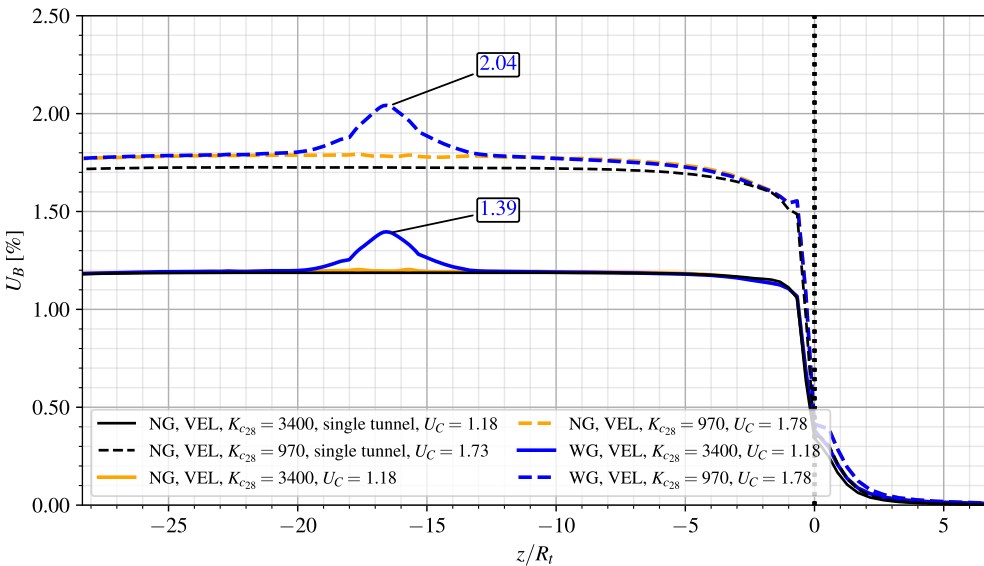


Figure 33: Effect of instantaneous lining stiffness on the long-term convergence profiles for the configuration of twin tunnels with and without transverse gallery and distance between twin tunnels $d_1 = 4R_t$ - elastoplastic-viscoplastic rock mass with viscoelastic lining.

Even in the specific case of $d_1 = 4R_t$ where a strong twin tunnels interaction would be expected, the role of lining with higher stiffness on stabilized convergence (blue and yellow solid lines in Fig. 33) is predominating with

values close to obtained for single tunnel (black solid line in Fig. 33), thus masking such interaction effect. For lower lining stiffness, the numerical results (blue and yellow dashed lines) indicate a small increase in the value of U_C when compared to the single tunnel (black dashed line).

As regards the impact on the peak convergence U_{peak} and extent of the gallery influence zone (disturbed portion of convergence profile), the results show that for each value of twin tunnels spacing d_1 , the latter extent is slightly affected by the instantaneous lining stiffness modulus. In contrast the ratio $(U_{peak} - U_C)/U_C$ is significantly affected by the values of d_1 and K_{c28} . For the configuration with $d_1 = 4R_t$, it respectively takes the values $(U_{peak} - U_C)/U_C = 14.5\%$ and 18% lower and higher lining stiffness, whereas it respectively takes the values 9.5% and 13% for the configuration with $d_1 = 16R_t$.

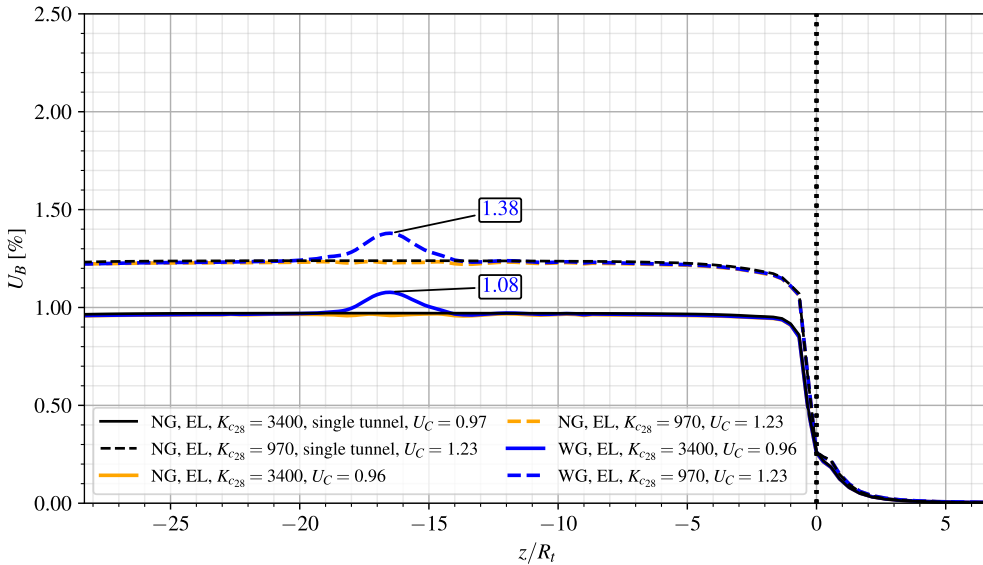


Figure 34: Effect of lining stiffness on the long-term convergence profiles for the configuration of twin tunnels with and without transverse gallery and distance between twin tunnels $d_1 = 16R_t$ - elastoplastic-viscoplastic rock mass with elastic lining.

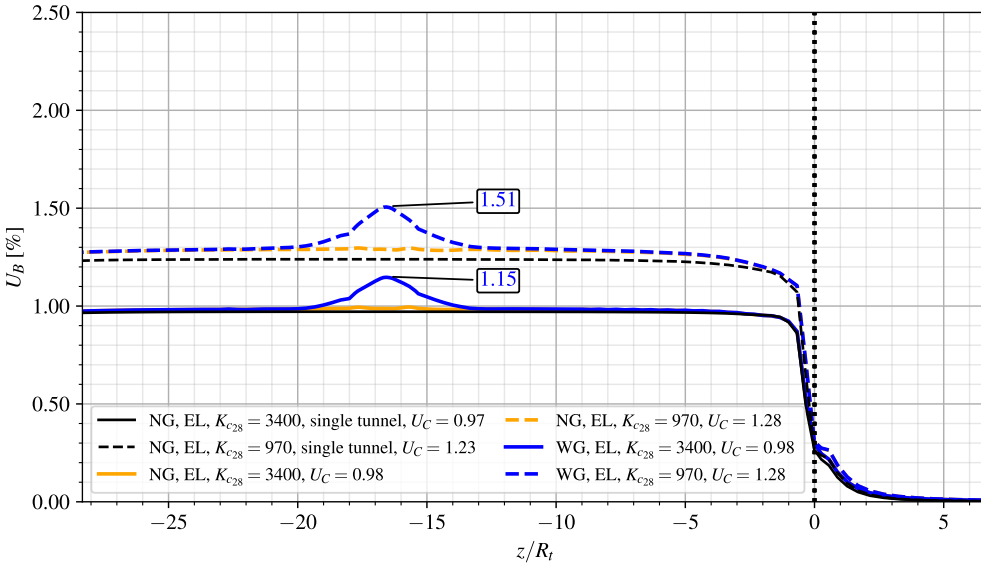


Figure 35: Effect of lining stiffness on the long-term convergence profiles for the configuration of twin tunnels with and without transverse gallery and distance between twin tunnels $d_1 = 4R_t$ - elastoplastic-viscoplastic rock mass with elastic lining.

Overall, the same observations formulated in the previous analyses regarding the effect of twin tunnel spacing on stabilized convergence still hold: with respect to single tunnel configuration, U_C is almost unaffected by the lining stiffness for U_C and slightly increased (up to 4%) for $d_1 = 4R_t$.

With the elastic lining, the increase in stiffness from $K_{c28} = 970$ MPa to $K_{c28} = 3400$ MPa leads to a reduction in stabilized convergence U_C by 28% for twin tunnels spacing $d_1 = 16R_t$ and by 16% for $d_1 = 4R_t$, emphasizing once again the strong mechanical interaction between the different components of the tunnel structure.

The peak value of tunnel roof convergence U_{peak} that reflects the coupling associated with intersecting transverse gallery is almost unaffected by the lining stiffness, at least for considered data parameters. In that respect, the value of ratio $(U_{peak} - U_C)/U_C$ computed in the configuration $d_1 = 16R_t$ (resp. $d_1 = 4R_t$) is approximately 12% (resp. and 18%) for both values of lining stiffness, which corroborates the predominating effect of tunnels proximity on peak convergence U_{peak} .

8. Conclusions

The paper presented a constitutive and computational model for addressing the deformation processes and mechanical interactions in deep twin tunnels with connecting transverse gallery. From the constitutive viewpoint, the irreversible component of rock deformation is modeled within the context of coupled plasticity–viscoplasticity. The latter framework is particularly relevant to describe both instantaneous and delayed deformation in deep clayey rocks. Emphasis has been devoted to the formulation of aging time-dependent constitutive properties of the lining constituent material with account for shrinkage and creep deformation, which are fundamental components of early age and long-term behavior of shotcrete support. At the structure level, the computational modeling integrates the nonlinear and time-dependent constitutive features with implementation of the activation-deactivation technique for simulating the processes of excavation and lining installation. The elaborated model is specifically devised for dealing with three-dimensional finite element analysis of deformation in twin tunnels/transverse gallery system, notably in the perspective of providing technical guidance for safe design of tunnel-gallery junction.

Conceived to provide preliminary insight into the impact of some relevant parameters defining the interaction problem, the numerical simulations undertaken in section 7 notably emphasized that:

- (a) The deformation anisotropy of the tunnel wall induced by twin tunnel proximity can be significant at both short-term and long-term deformation even when a stiff lining is used. This feature should therefore be integrated in the support design stage.
- (b) The disturbed region with localized extent near the tunnel-gallery junction, reflecting the strong interaction between these two components of the structure, exhibits peak convergence values that can exceed by a large amount that the convergence far behind the facing. In that respect, the study presents the potential to formulate technical guidance for the design of twin tunnels with transverse gallery.
- (c) In addition to the effects of coupled plastic-viscoplastic constitutive properties of the rock material, the aging time-dependent behavior considered for the lining concrete/shotcrete has a considerable impact on the short-term and long-term convergence profiles of the tunnel. In particular, the aging viscoelastic lining reveals more efficient in controlling the long-term tunnel convergence than that at short term, which is mainly attributed to the early age properties of constituent material.

Even though the numerical simulations have mainly concerned the situation of deep circular tunnels, the constitutive and related computational model can in its current version be readily applied to analyze more complex configuration exhibiting no particular symmetries as that examined in this paper. In that respect, the following developments may be foreseen in the immediate future:

- (a) The simulation of shallow depth twin tunnels connected or not by transverse galleries, commonly encountered in the urban underground environment and for which the initial stress state should be beforehand properly evaluated. In particular, the modeling should address deformation and design of shallow twin tunnels excavated in horizontal parallel profiles or stacked over each other (e.g., [Islam and Iskander (2021), Do et al. (2022, Chakeri et al. (2011), Do et al. (2016), Do et al. (2014), Do et al. (2015)].)
- (b) An important aspect to be integrated in the simulations and interaction assessment is related to more realistic tunneling scenario, describing the sequential excavation phase of each component of the underground structure as well as that of the lining placement. A significant impact of the lagged tunnel construction procedure, and more specifically the lagging distance between the faces of twin tunnels as well as of transverse galleries, is notably expected due the time-depend behavior of constituent materials [Islam and Iskander (2021), Do et al. (2016), Ng et al, (2004)]. The numerical modeling and analysis of such configurations is currently the object of ongoing research.

Finally, it should be kept in mind that effective validation of the constitutive and computational modeling remains to be achieved through comparison of the numerical predictions with available experimental and monitoring field data.

References

- [1] Chortis F, Kavvadas M. Three-dimensional numerical investigation of the interaction between twin tunnels. *Geotechnical and Geological Engineering* 2021;39:5559–5585. doi:<https://doi.org/10.1007/s10706-021-01845-5>.
- [2] Brenner Base Tunnel – interaction between underground structures, complex challenges and strategies. In: *Tunnels and Underground Cities: Engineering and Innovation meet Archaeology, Architecture and Art*; 1 ed. CRC Press; 2019, p. 3857–3865. doi:[10.1201/9780429424441-408](https://doi.org/10.1201/9780429424441-408).
- [3] Pöttler R. Three-dimensional modelling of junctions at the Channel Tunnel project. *International Journal for Numerical and Analytical Methods in Geomechanics* 1992;16(9):683–695. doi:[10.1002/nag.1610160906](https://doi.org/10.1002/nag.1610160906).
- [4] Nyren R. Field measurements above twin tunnels in London Clay. Ph.D. Thesis; Imperial College London (University of London); London, England; 1998. URL: <http://spiral.imperial.ac.uk/handle/10044/1/8573>.
- [5] Hsiao F, Chi-Wen YU, Chern J. Modeling the behaviors of the tunnel intersection areas adjacent to the ventilation shafts in the Hsuehshan tunnel. In: Proceedings of the international symposium on design, construction and operation of long tunnels, Taipei. 2005, URL: <https://www.semanticscholar.org/paper/MODELING-THE-BEHAVIORS-OF-THE-TUNNEL-INTERSECTION-Hsiao-Chi-Wen-3a8f5327a1ef5e206f76657e5fc4b10865947987>.
- [6] Three-dimensional analysis of tunnel intersections for a train tunnel under Stockholm. In: *Proceedings of the North American Tunneling 2006 Conference*. ????,
- [7] Karakus M, Ozsan A, Başarır H. Finite element analysis for the twin metro tunnel constructed in Ankara Clay, Turkey. *Bulletin of Engineering Geology and the Environment* 2007;66(1):71–79. doi:[10.1007/s10064-006-0056-z](https://doi.org/10.1007/s10064-006-0056-z).
- [8] Afifipour M, Sharifzadeh M, Shahriar K, Jamshidi H. Interaction of twin tunnels and shallow foundation at Zand underpass, Shiraz metro, Iran. *Tunnelling and Underground Space Technology* 2011;26(2):356–363. doi:[10.1016/j.tust.2010.11.006](https://doi.org/10.1016/j.tust.2010.11.006).
- [9] Fortsakis P, Bekri E, Prountzopoulos G, Marinos P. Numerical analysis of twin tunnels interaction. In: *Proc. 1st Eastern European Tunnelling Conference*. Budapest, Hungary; 2012.,

- [10] Fargnoli V, Boldini D, Amorosi A. Twin tunnel excavation in coarse grained soils: Observations and numerical back-predictions under free field conditions and in presence of a surface structure. *Tunnelling and Underground Space Technology* 2015;49:454–469. doi:[10.1016/j.tust.2015.06.003](https://doi.org/10.1016/j.tust.2015.06.003).
- [11] Li Y, Jin X, Lv Z, Dong J, Guo J. Deformation and mechanical characteristics of tunnel lining in tunnel intersection between subway station tunnel and construction tunnel. *Tunnelling and Underground Space Technology* 2016;56:22–33. doi:[10.1016/j.tust.2016.02.016](https://doi.org/10.1016/j.tust.2016.02.016).
- [12] Elwood DEY, Martin CD. Ground response of closely spaced twin tunnels constructed in heavily overconsolidated soils. *Tunnelling and Underground Space Technology* 2016;51:226–237. doi:[10.1016/j.tust.2015.10.037](https://doi.org/10.1016/j.tust.2015.10.037).
- [13] Wan MSP, Standing JR, Potts DM, Burland JB. Measured short-term ground surface response to EPBM tunnelling in London Clay. *Géotechnique* 2017;67(5):420–445. doi:[10.1680/jgeot.16.P.099](https://doi.org/10.1680/jgeot.16.P.099).
- [14] Spyridis P, Bergmeister K. Analysis of lateral openings in tunnel linings. *Tunnelling and Underground Space Technology* 2015;50:376–395. doi:[10.1016/j.tust.2015.08.005](https://doi.org/10.1016/j.tust.2015.08.005).
- [15] Nemat-Nasser S, Hori M. Micromechanics: overall properties of heterogeneous materials. North-Holland; 1993.
- [16] Deudé V, Dormieux L, Kondo D, Maghous S. Micromechanical approach to nonlinear poroelasticity: Application to cracked rocks. *Journal of Engineering Mechanics* 2002;128(8):848–855. doi:[https://doi.org/10.1061/\(ASCE\)0733-9399\(2002\)128:8\(848\)](https://doi.org/10.1061/(ASCE)0733-9399(2002)128:8(848)).
- [17] de Buhan P, Fréard J, Garnier D, Maghous S. Failure properties of fractured rock masses as anisotropic homogenized media. *Journal of Engineering Mechanics* 2002;128(8):869–875. doi:[https://doi.org/10.1061/\(ASCE\)0733-9399\(2002\)128:8\(869\)](https://doi.org/10.1061/(ASCE)0733-9399(2002)128:8(869)).
- [18] Marmier R, Jeannin L, Barthélémy JF. Homogenized constitutive laws for rocks with elastoplastic fractures. *International Journal for Numerical and Analytical Methods in Geomechanics* 2007;31(10):1217–1237. doi:<https://doi.org/10.1002/nag.595>.
- [19] Aguiar CB, Maghous S. A micromechanics-based approach to damage propagation criterion in viscoelastic fractured materials regarded as homogenized media. *International Journal for Numerical and Analytical Methods in Geomechanics* 2023;47(6):936–971. doi:<https://doi.org/10.1002/nag.3500>.
- [20] Rousset G. Comportement mécanique des argiles profondes: Application au stockage de déchets radioactifs. Ph.D. Thesis (in french); Ecole Nationale des Ponts et Chaussées; Paris, France; 1988. URL: <http://www.theses.fr/1988ENPCA005>.
- [21] Nguyen Minh D, Rousset G. Influence of instantaneous failure on time dependent behavior of underground galleries. In: The 28th U.S. Symposium on Rock Mechanics (USRMS). Tucson, Arizona; 1987, p. ARMA-87-0663.
- [22] Giraud A, Rousset G. Time-dependent behaviour of deep clays. *Engineering Geology* 1996;41(1):181–195. doi:[https://doi.org/10.1016/0013-7952\(95\)00000-3](https://doi.org/10.1016/0013-7952(95)00000-3).
- [23] Bernaud D, Rousset G. L'essai de soutènement à convergence contrôlée. In: Proc. of International Symposium, Geotechnical Engineering of Hard Soils-Soft Rocks. Athens; 1993, p. 1381–1391.
- [24] Piepi GT. Comportement viscoplastique avec rupture des argiles raides. applications aux ouvrages souterrains. Ph.D. Thesis (in french); Ecole Nationale des Ponts et Chaussées; Paris, France; 1995. URL: <https://pastel.hal.science/tel-00523616/document>.
- [25] Quevedo FPM. Análise computacional das deformações em túneis profundos considerando o acoplamento plasticidade-viscoplasticidade. Ph.D. Thesis (in portuguese); Federal University of Rio Grande do Sul; Porto Alegre, Brazil; 2021. URL: <https://lume.ufrgs.br/handle/10183/239617>.
- [26] Quevedo FPM, Bernaud D, Maghous S. Numerical integration scheme for coupled elastoplastic–viscoplastic constitutive law for tunnels. *International Journal of Geomechanics* 2022;22(10). doi:[https://doi.org/10.1061/\(ASCE\)GM.1943-5622.0002512](https://doi.org/10.1061/(ASCE)GM.1943-5622.0002512).
- [27] Bernaud D. Tunnels profonds dans les milieux viscoplastiques: approches expérimentale et numérique. Ph.D. Thesis (in french); Ecole Nationale des Ponts et Chaussées; Paris, France; 1991. URL: <https://theses.hal.science/tel-00529719/>.
- [28] Perzyna P. Fundamental problems in viscoplasticity. In: Advances in applied mechanics; vol. 9. Elsevier; 1966, p. 243–377.
- [29] Bažant ZP, Prasannan S. Solidification theory for concrete creep. I: Formulation. *Journal of Engineering Mechanics* 1989;115(8):1691–1703. doi:[https://doi.org/10.1061/\(ASCE\)0733-9399\(1989\)115:8\(1691\)](https://doi.org/10.1061/(ASCE)0733-9399(1989)115:8(1691)).
- [30] Bažant ZP, Prasannan S. Solidification theory for concrete creep. II: Verification and application. *Journal of Engineering Mechanics* 1989;115(8):1704–1725. doi:[https://doi.org/10.1061/\(ASCE\)0733-9399\(1989\)115:8\(1704\)](https://doi.org/10.1061/(ASCE)0733-9399(1989)115:8(1704)).
- [31] CEB-FIP. CEB-FIP model code 1990: Design code. Comité Euro International du Béton and Fédération Internationale de la Précontrainte (CEB-FIP); 1993.
- [32] Quevedo FPM, Schmitz RJ, Morsch IB, A. CF, Bernaud D. Customization of a software of finite elements to analysis of concrete structures: long-term effects. *IBRACON Structures and Materials Journal* 2018;11(4):696–718. doi:<https://doi.org/10.1590/S1983-41952018000400005>.
- [33] Quevedo FPM, Bernaud D, Campos Filho A. Numerical analysis of deep tunnels in viscoplastic rock mass considering the creep and shrinkage of the concrete lining. *International Journal of Geomechanics* 2022;22(4). doi:[https://doi.org/10.1061/\(ASCE\)GM.1943-5622.0002282](https://doi.org/10.1061/(ASCE)GM.1943-5622.0002282).
- [34] Quevedo FPM. Comportamento a longo prazo de túneis profundos revestidos com concreto: modelo em elementos finitos. Master Thesis (in portuguese); Federal University of Rio Grande do Sul; Porto Alegre, Brazil; 2017. URL: <https://lume.ufrgs.br/handle/10183/163886>.
- [35] Bernaud D, Debuhau P, Maghous S. Numerical-simulation of the convergence of a bolt-supported tunnel through a homogenization method. *International Journal for Numerical and Analytical Methods in Geomechanics* 1995;19(4):267–288. doi:<https://doi.org/10.1002/nag.1610190404>.
- [36] Bernaud D, Maghous S, Debuhau P, Couto E. A numerical approach for design of bolt-supported tunnels regarded as homogenized structures. *Tunneling and underground space technology* 2009;24(5):533–546. doi:<https://doi.org/10.1016/j.tust.2009.02.002>.
- [37] Maghous S, Bernaud D, Couto E. Three-dimensional numerical simulation of rock deformation in bolt-supported tunnels: A homogenization approach. *Tunneling and Underground Space Technology* 2012;31:267–288. doi:<https://doi.org/10.1016/j.tust.2012.04.008>.
- [38] Zienkiewicz O, Cormeau I. Visco-plasticity—plasticity and creep in elastic solids—a unified numerical solution approach. *International Journal for Numerical Methods in Engineering* 1974;8(4):821–845. doi:<https://doi.org/10.1002/nme.v8:4>.

- [39] Simo JC, Hughes TJR. Computational Inelasticity. Springer-Verlag; 1998.
- [40] Guo Z, Liu X, Zhu Z. An elastic solution for twin circular tunnels' stress in hydrostatic stress field. Geotechnical and Geological Engineering 2021;39:1–11. doi:<https://doi.org/10.1007/s10706-021-01756-5>.
- [41] Ling CB. On the stresses in a plate containing two circular holes. Journal of Applied Physics 1948;19(1):77–82. doi:<https://doi.org/10.1063/1.1697875>.
- [42] Ma Y, Lu A, Zeng X, Cai H. Analytical solution for determining the plastic zones around twin circular tunnels excavated at great depth. International Journal of Rock Mechanics and Mining Sciences 2020;136:104475. doi:<https://doi.org/10.1016/j.ijrmms.2020.104475>.
- [43] Giraud A. Couplages thermo-hydro-mécaniques dans les poreux peu perméables: application aux argiles profondes. Ph.D. Thesis (in french); Ecole Nationale des Ponts et Chaussées; Paris, France; 1993. URL: <https://theses.fr/1993ENPC9310>.
- [44] Panet M. Le Calcul des Tunnels par la Méthode Convergence-Confinement. Presses De L'école Nationale Des Ponts Et Chaussees; 1995. ISBN 2859782303.
- [45] Hoek E, Brown ET. Underground excavations in rock. CRC Press; 1980.